Copy
RM L58A28

NACA

RESEARCH MEMORANDUM

DYNAMIC DIRECTIONAL STABILITY DERIVATIVES FOR A 45° SWEPT-WING—VERTICAL-TAIL AIRPLANE MODEL AT TRANSONIC SPEEDS AND ANGLES OF ATTACK, WITH A DESCRIPTION OF THE MECHANISM AND INSTRUMENTATION EMPLOYED

By Albert L. Braslow, Harleth G. Wiley, and Cullen Q. Lee

Langley Aeronautical Laboratory
Langley Field, Va.

NATIONAL ADVISORY COMMITTEE
FOR AERONAUTICS

WASHINGTON
April 21, 1958

[redacted]

NACA RM L58A28

NATIONAL ADVISORY COMMITTEE FOR AERONAUTICS

RESEARCH MEMORANDUM

DYNAMIC DIRECTIONAL STABILITY DERIVATIVES FOR A 45° SWEPT-WING—VERTICAL-TAIL AIRPLANE MODEL AT TRANSONIC SPEEDS AND ANGLES OF ATTACK, WITH A DESCRIPTION OF THE MECHANISM AND INSTRUMENTATION EMPLOYED

By Albert L. Braslow, Harleth G. Wiley, and Cullen Q. Lee

SUMMARY

Measurements were made of the aerodynamic damping in yaw and oscillatory directional stability for a 45° sweptback-wing—vertical-tail airplane model at transonic speeds. The model was oscillated approximately ±1° about the vertical body axis at the quarter-chord of the wing mean aerodynamic chord for a range of reduced-frequency parameter from 0.030 to 0.057. Tests were made at angles of attack from 0° to about $12\frac{1}{2}^\circ$ through a Mach number range from about 0.78 to 1.30. Reynolds numbers for the tests, based on wing mean aerodynamic chord, were approximately 1.5×10^6 and 2.5×10^6.

Results of the tests show that the damping-in-yaw derivative was independent of angle of attack up to an angle of attack of $12\frac{1}{2}^\circ$ at subsonic Mach numbers. At Mach numbers above 0.95, the damping was increased markedly at 5° angle of attack over that at 0° angle of attack with further increases evident with increased Mach number and angle of attack. The oscillatory directional stability parameter decreased with angle of attack for angles of attack above 5° for Mach numbers from 0.95 to 1.30.

The tests were made on a sting-mounted model which was rigidly forced to perform a known single-degree-of-freedom angular oscillation. The measured dynamic stability derivatives were uninfluenced by turbulence and buffeting.

INTRODUCTION

Design of guidance and control systems for airplanes and missiles requires knowledge of the various dynamic stability derivatives through wide ranges of flight speed. Experimental data and theories are available at low speeds and a limited amount of such information is available at supersonic speeds. At transonic speeds, however, no adequate theories for predicting these derivatives are available and there exist little experimental data.

Low-speed tests have revealed some important trends of dynamic stability derivatives; for example, a large increase in the aerodynamic damping-in-yaw derivative $C_{n_r} - C_{n_{\dot{\beta}}}$ has been measured at large values of angle of attack for wings with leading-edge sweep (refs. 1 and 2). This low-speed increase in damping, which was attributed to flow separation at large angles of attack, raised the question as to whether shock-induced boundary-layer separation at transonic speeds might produce similar effects at lower angles of attack. An investigation of the effect of angle of attack on this damping at transonic speeds therefore was made.

The investigation was made in the Langley transonic blowdown tunnel on a 45° sweptback-wing—vertical-tail—fuselage configuration. The model was oscillated approximately ±1° about the vertical body axis at the quarter-chord of the wing mean aerodynamic chord for a range of reduced-frequency parameter from 0.030 to 0.057. Tests were made at angles of attack of 0°, 5°, and 8° through a Mach number range from about 0.78 to 1.30 with a few tests at angles of attack of 10° and 12.5° for Mach numbers up to 1.02. The Reynolds numbers based on wing mean aerodynamic chord were approximately 1.5×10^6 and 2.5×10^6.

Three techniques of measuring dynamic stability of models in wind tunnels are presently available. The first technique involves the measurement of the decaying free oscillations of a model mounted on a suitable elastic restraint with a single degree of freedom. (For example, see refs. 3 and 4.) The second technique is that of self-excitation, in which a model is driven through a spring in a single degree of freedom and the amplitude of oscillation is controlled by a feedback loop. (For example, see ref. 5.) Dynamic stability is determined by measuring the force required to maintain the stabilized oscillation. The third technique is termed the inexorable method in which the model is rigidly forced to oscillate in a single degree of freedom at fixed amplitude and frequency while measurements are made of the force required to sustain the motion. For example, this technique was used for low-speed, low-frequency tests and is reported in reference 6.

[redacted]

A mechanism for accurately measuring dynamic stability at transonic or supersonic speeds must meet several stringent design requirements which generally are not so severe at low speeds. Foremost is the problem of accurately separating the relatively small aerodynamic forces which are due to the model motion from the large forces imposed on the system by inertia effects and static aerodynamic loads. The inertia loads are usually large compared with those at low speeds because of the need to oscillate at high frequencies in order to maintain realistic values of reduced frequency. Secondly, the measured dynamic stability must not be influenced by extraneous energy sources, such as airstream turbulence and buffeting. Reference 3, for example, shows how airstream turbulence can influence the model motion and, therefore, the measured dynamic stability of a configuration performing free oscillations. Thirdly, the models must be sting-mounted to minimize model support interference. All primary mechanical and electrical equipment required to operate the model, therefore, must be enclosed in the limited space available in the model and sting support. Because of these space limitations and the large aerodynamic loads imposed, the design of such items as the oscillating model pivot becomes quite critical.

An inexorable or rigidly forced system has been developed for the present tests to measure the aerodynamic damping and oscillatory directional stability about the vertical body axis of a sting-mounted model at transonic and supersonic speeds. The system fulfills the foregoing requirements for measuring the dynamic stability of a model at transonic and supersonic speeds. Descriptions of the mechanism and instrumentation used are included in the appendixes of this report.

SYMBOLS

All aerodynamic coefficients in this paper are presented in the body system of axes and all moments are referred to the vertical oscillation axis which is in the plane of symmetry at the quarter-chord of the mean aerodynamic chord.

b wing span

c wing chord

$\bar{c}$ wing mean aerodynamic chord, $\frac{2}{S}\int_0^{b/2} c^2 dy$

k reduced-frequency parameter referred to semispan of wing, $\frac{\omega b}{2V}$

[redacted]

M	Mach number
N	yawing moment
p_t	tunnel total pressure
q	dynamic pressure, $\frac{1}{2}\rho V^2$
r	angular velocity in yaw, $\frac{\partial \psi}{\partial t}$, radians/sec
$\dot{r}$	yawing acceleration, $\frac{\partial^2 \psi}{\partial t^2}$, radians/sec^2
R	Reynolds number based on $\bar{c}$
S	wing area
t	time, sec
V	free-stream velocity
α	angle of attack, deg
β	angle of sideslip (measured to plane of symmetry and in plane of relative wind), radians
$\dot{\beta} = \frac{\partial \beta}{\partial t}$	
ψ	instantaneous yaw angle, radians
ρ	mass density of air
ω	angular frequency of oscillation, radians/sec
C_n	yawing-moment coefficient, $\frac{N}{qSb}$
$C_{n_r} = \frac{\partial C_n}{\partial\left(\frac{\omega b}{2V}\right)}$	

[redacted]

$$C_{n_{\dot{r}}} = \frac{\partial C_n}{\partial\left(\frac{\dot{r}b^2}{4V^2}\right)}$$

$$C_{n_\beta} = \frac{\partial C_n}{\partial \beta}$$

$$C_{n_{\dot{\beta}}} = \frac{\partial C_n}{\partial\left(\frac{\dot{\beta}b}{2V}\right)}$$

The subscript ω denotes data obtained by oscillation tests.

APPARATUS

The system developed for determining aerodynamic damping and oscillatory stability for the present investigation utilized the technique of measuring the moment required to drive the model at known amplitudes and frequencies of oscillation. A description of the principles involved and the instrumentation required is included in appendix A.

The mechanism used for these tests consisted of a sting-mounted model which was forced to perform a single-degree-of-freedom oscillation about its vertical axis (fig. 1). The model was driven by a hydraulic pump and a constant-speed electric motor which were mounted outside the tunnel (fig. 2). The natural frequency of the model system was varied by the use of frequency springs of various stiffnesses. Photographs of the model, mechanisms, and instrumentation are shown as figures 3, 4, and 5. Complete details of the hardware are included in appendix B.

In operation of the system, calibrated outputs of moment and displacement strain gages are passed through coupled electrical sine-cosine resolvers which rotate at the frequency of oscillation (figs. 2, 3, and 4). The resolvers transform the moment and amplitude functions into orthogonal components which are simultaneously measured on direct-current microammeters (fig. 5). From these components the applied moment and displacement and the phase angle between them can be found, and with the known oscillation frequency the aerodynamic-damping and oscillatory-directional-stability moments can be computed. For maximum accuracy, the system is operated at or very near the natural frequency of the model system. (See appendix A.)

[redacted]

The model was mounted on a sting-support mechanism which permitted testing at angles of attack up to $12\frac{1}{2}^{\circ}$ while maintaining model location approximately on the wind-tunnel center line. A fouling light circuit was arranged to indicate contact between the model base and sting (fig. 5) and tests were not made when this condition existed.

MODEL

A sketch of the model tested is presented in figure 6. The model had a steel wing with 45° sweepback at the quarter chord, an aspect ratio of 4.0, a taper ratio of 0.3, and an NACA 65A006 airfoil section parallel to the stream. The wing was mounted on the fuselage center line and had no dihedral or twist. The vertical tail was made of brass and had 45° sweepback at the quarter-chord, an aspect ratio of 2.0, a taper ratio of 0.3, and an NACA 65A006 airfoil parallel to the stream. No horizontal tail was used. The fuselage was a simple body of revolution with a fineness ratio of 7. The removable nose was made of aluminum and the remainder of the fuselage was made of Phosphor bronze with a removable upper section (fig. 3). The center of gravity of the model was coincident with the vertical axis of rotation which was in the plane of symmetry at the quarter-chord of the mean aerodynamic chord.

TESTS

The tests were made in the Langley transonic blowdown tunnel, which has a slotted octagonal test section with 26 inches between flats. Tests were made through a Mach number range from about 0.78 to 1.30. Previous experience had indicated that aerodynamic characteristics of models of the present size are affected by the intersection of wall-reflected disturbances with the model in the Mach number range between about 1.04 and 1.13. No data are presented, therefore, for this Mach number range.

The tests were made at tunnel stagnation pressures of approximately 30 and 50 pounds per square inch absolute with corresponding Reynolds numbers, based on wing mean aerodynamic chord, of about 1.5×10^6 and 2.5×10^6, respectively (fig. 7). The results of reference 7 indicate that, for the Reynolds number range of the present investigation, it is extremely unlikely that the model surface condition was smooth enough to permit attainment of laminar boundary-layer flow.

Measurements were made of the damping-in-yaw parameter $C_{n_{r,\omega}} - C_{n_{\dot{\beta},\omega}}$ and the oscillatory directional stability derivative $C_{n_{\beta,\omega}} + k^2 C_{n_{\dot{r},\omega}}$ at angles of attack of 0°, 5°, and 8° throughout most of the Mach number range for a stagnation pressure of 30 pounds per square inch absolute. Additional tests were made at 10° angle of attack up to Mach numbers of about 1.02 and at $\alpha = 12\frac{1}{2}^\circ$ for Mach numbers up to 0.87. Tests at a stagnation pressure of 50 pounds per square inch absolute were restricted to angles of attack of 0° and 5° because of high lift loads on the model. The reduced-frequency parameter $\frac{\omega b}{2V}$ varied from 0.030 to 0.057 for the tests.

ACCURACY

Ability of the force-driven mechanism to measure damping in yaw was determined by applying a known damping moment while oscillating the model. The model wings were replaced by dummy wings of sheet copper, which oscillated between the poles of a double electromagnet (fig. 8). When the electromagnet coils were energized, eddy-current losses set up in the copper plate were proportional to the oscillatory velocity of the plate and applied a damping moment to the model. With the drive piston removed, the value of damping moment applied to the model by the eddy-current damper was measured by the well-known free-decay technique for various values of current applied to the electromagnet. With the drive piston replaced, the model was forced to oscillate with similar applied eddy-current moments and the moments were measured by the technique used in this investigation. Agreement between the results of the two methods of measuring damping moments was excellent (fig. 9).

The results presented in this report include results of intentional repetition of test conditions during four separate tests. Throughout the tests, experiments of technique were continually made to improve data accuracy by reducing the value of internal or tare damping, improving flexure pivot characteristics, increasing instrumentation response, and improving oscillation frequency control. The data presented for the four tests, therefore, contain scatter which was attendant to the continual development of the method of testing. Based on repeatability throughout the full program of the tests, the accuracy of measuring the derivative $C_{n_{r,\omega}} - C_{n_{\dot{\beta},\omega}}$ was about ± 0.08 and the accuracy of measuring $C_{n_{\beta,\omega}} + k^2 C_{n_{\dot{r},\omega}}$ was about ± 0.03. Accuracy of measuring Mach number was about ± 0.01 and of measuring angle of attack was about $\pm 0.2^\circ$.

[redacted]

RESULTS AND DISCUSSION

The variation of the damping-in-yaw derivative $C_{n_{r,\omega}} - C_{n_{\dot{\beta},\omega}}$ with Mach number for various frequency springs, angles of attack, and tunnel stagnation pressures is presented in figure 10. (The frequency springs are hereafter referred to as springs 1, 2, and 3, respectively, in order of decreasing stiffness.) The variation of $C_{n_{\beta,\omega}} + k^2 C_{n_{\dot{r},\omega}}$ with Mach number is presented in figure 11. Cross plots of $C_{n_{r,\omega}} - C_{n_{\dot{\beta},\omega}}$ and $C_{n_{\beta,\omega}} + k^2 C_{n_{\dot{r},\omega}}$ as a function of angle of attack for various Mach numbers are presented in figure 12. Reduced-frequency parameter $\frac{\omega b}{2V}$ for the tests is presented as a function of Mach number in figure 13.

At 0° angle of attack, $C_{n_{r,\omega}} - C_{n_{\dot{\beta},\omega}}$ increased negatively with Mach number between $M = 0.9$ and $M = 1.2$ and remained approximately constant at the higher Mach numbers for all frequency springs and stagnation pressures tested (fig. 10). The absolute value of $C_{n_{r,\omega}} - C_{n_{\dot{\beta},\omega}}$ remained about the same (within the accuracy of the data) for all oscillation frequencies tested. At angles of attack of 5° and above, the magnitude of $C_{n_{r,\omega}} - C_{n_{\dot{\beta},\omega}}$ increased rapidly with Mach number at Mach numbers above about 0.9 for tests with spring 1 (fig. 10(a)). A cross plot of $C_{n_{r,\omega}} - C_{n_{\dot{\beta},\omega}}$ with angle of attack (fig. 12) shows that, at a subsonic Mach number of 0.87, the value of $C_{n_{r,\omega}} - C_{n_{\dot{\beta},\omega}}$ is independent of angle of attack up to at least $\alpha = 12\frac{1}{2}^\circ$, which substantiates trends found at low speeds for swept wings (refs. 1 and 2). At a Mach number of 0.95, however, the damping in yaw had increased at $\alpha = 5^\circ$ to about twice that at $\alpha = 0^\circ$ but had decreased for $\alpha = 8^\circ$ and $\alpha = 10^\circ$ to the level obtained at $\alpha = 0^\circ$. At Mach numbers above 0.95, $C_{n_{r,\omega}} - C_{n_{\dot{\beta},\omega}}$ had increased at all angles of attack above 5°. References 1 and 2 show a sharp increase in damping in yaw at angles of attack of about 14° for swept wings at low speeds; this increase was attributed to flow separation on swept wings at these angles of attack. The increase in $C_{n_{r,\omega}} - C_{n_{\dot{\beta},\omega}}$ for the present tests appears to occur at much lower angles of attack for high subsonic and supersonic speeds (fig. 12) and may be attributed to shock-induced separation at the higher Mach numbers. How flow separation increases the damping in yaw is not immediately apparent, but the phenomenon may result from a time lag in the effects of separation from each wing (ref. 2).

The oscillatory directional stability parameter $C_{n_{\beta,\omega}} + k^2 C_{n_{\dot{r},\omega}}$ generally increased with Mach number at $\alpha = 0^\circ$ up to $M = 1.2$ and decreased with further increase in Mach number (fig. 11). At a subsonic Mach number of 0.87 (fig. 12), the value of $C_{n_{\beta,\omega}} + k^2 C_{n_{\dot{r},\omega}}$ remained fairly constant with angle of attack up to $\alpha = 8^\circ$ and increased at the higher angles of attack. Above $M = 0.95$, $C_{n_{\beta,\omega}} + k^2 C_{n_{\dot{r},\omega}}$ decreased with angle of attack above $\alpha = 5^\circ$.

CONCLUDING REMARKS

Wind-tunnel tests were made of the aerodynamic damping in yaw and oscillatory directional stability at transonic speeds of a 45° sweptback-wing—vertical-tail airplane model. The tests were made at Mach numbers from 0.78 to 1.30 and at angles of attack from 0° to about $12\frac{1}{2}^\circ$. The model was oscillated in yaw approximately $\pm 1^\circ$ about its vertical body axis at the quarter-chord of the mean aerodynamic chord for a range of reduced-frequency parameter $\frac{\omega b}{2V}$ from 0.030 to 0.057. The Reynolds numbers, based on wing mean aerodynamic chord, were about 1.5×10^6 and 2.5×10^6.

Results of the tests show that the damping-in-yaw derivative $C_{n_{r,\omega}} - C_{n_{\dot{\beta},\omega}}$ was independent of angle of attack at a subsonic Mach number of 0.87 up to an angle of attack of $12\frac{1}{2}^\circ$. At Mach numbers of 0.95 and above, $C_{n_{r,\omega}} - C_{n_{\dot{\beta},\omega}}$ had increased markedly at 5° angle of attack with further increases evident as Mach number and angle of attack were increased. The oscillatory directional stability parameter $C_{n_{\beta,\omega}} + k^2 C_{n_{\dot{r},\omega}}$ decreased with angle of attack for angles of attack above 5° for Mach numbers from 0.95 to 1.30.

The tests were made on a sting-mounted model which was rigidly forced to perform a known single-degree-of-freedom angular oscillation. The measured dynamic stability derivatives were uninfluenced by turbulence and buffeting.

Langley Aeronautical Laboratory,
National Advisory Committee for Aeronautics,
Langley Field, Va., January 8, 1958.

[redacted]

APPENDIX A

PRINCIPLES OF MEASURING DYNAMIC STABILITY BY THE FORCED-OSCILLATION TECHNIQUE

A discussion of the principles of measuring dynamic stability and of the methods involved are presented in this appendix. Mechanical application of these principles is discussed in appendix B. Additional symbols used in the equations of this appendix and not presented in the text are defined as follows:

τ	period of oscillation, sec
f	frequency, $1/\tau$, cycles/sec
ω_c	carrier frequency, radians/sec
M	applied moment, in-lb
ψ	maximum amplitude of yaw angle, radians
K	system spring constant, in-lb/radians
C	system damping, in-lb/radians/sec
λ	phase angle between applied moment and resolver axis, radians
δ	phase angle between angular displacement and resolver axis, radians
θ	phase angle between applied moment and angular displacement, radians
γ	phase angle between model axis and resolver axis, radians
i	instantaneous value of current, microamperes
$\bar{i}$	average value of current, microamperes
I_Z	moment of inertia about Z-axis, slug-ft^2
n	an integer (1,2,3, ...)
a	maximum transformation ratio of resolver

[redacted]

A calibration constant for moment or displacement, microamperes/in-lb or microamperes/radians

B calibration constant, volts/in-lb

e base of natural system of logarithms; or instantaneous value of voltage applied to resolver, volts

$j = \sqrt{-1}$

Subscripts:

aero aerodynamic characteristics

M moment

ψ displacement

r real component

j imaginary component

o constant component

1 fundamental component or fundamental frequency

n the nth component

In this method of measuring dynamic stability by the force-driven technique, the model is rigidly forced to perform a single-degree-of-freedom oscillation while measurements are made of the model motion and of the moment required to sustain the motion. The model, when oscillating in yaw only, can be likened to a simple single-degree-of-freedom mechanical system whose characteristics can be related by the differential equation

$$I\ddot{\psi} + C\dot{\psi} + K\psi = Me^{j(\omega t-\theta)}$$

A solution to this equation is

$$\left(-I_Z\omega^2 + jC\omega + K\right)\psi = Me^{j\theta} \qquad (A1)$$

The vector diagram of equation (A1) is shown in sketch 1 with the real axis alined with the displacement vector.

[redacted]

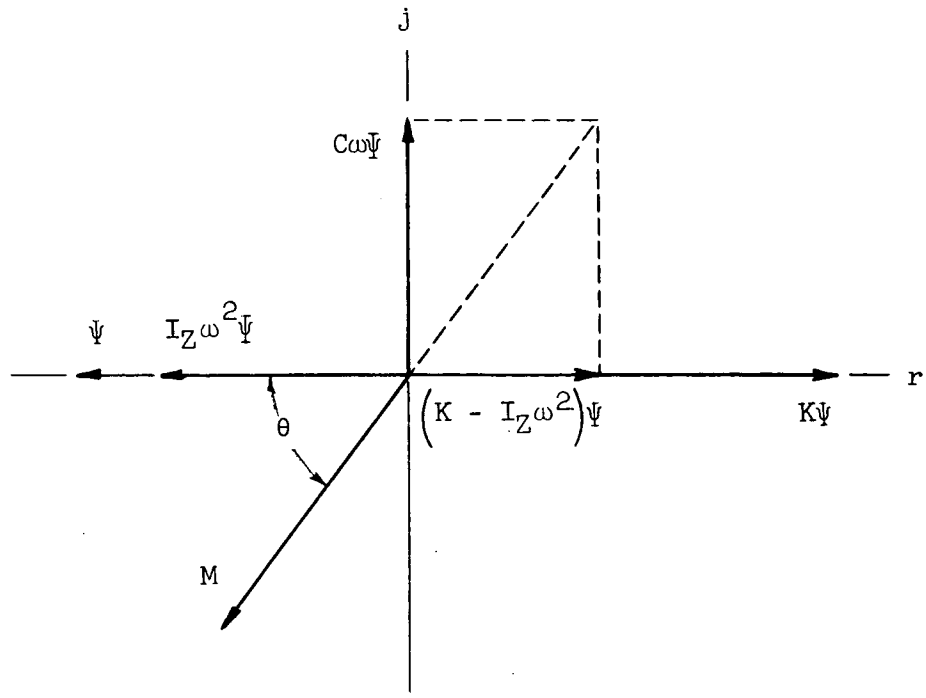

Sketch 1

From this diagram, the imaginary components may be equated to give

$$C\omega\psi = M \sin \theta$$

and the total system damping is

$$C = \frac{M \sin \theta}{\omega\psi} \tag{A2}$$

Similarly, the real components may be equated to give

$$K\psi - I_Z\omega^2\psi = M \cos \theta$$

and the total system spring constant is

$$K = \frac{M \cos \theta}{\psi} + I_Z\omega^2 \tag{A3}$$

[redacted]

Thus, if measurements are made of the applied moment M, the displacement ψ, the phase angle θ between M and ψ, and the angular velocity ω, the total system damping and spring constant can be computed.

A block diagram of the electronic circuit used to measure the applied moment is shown in figure 14. A similar circuit was used to measure the angular displacement.

The oscillator supplies a 10-volt, 3-kilocycle carrier voltage to the moment strain-gage bridge circuit. After the bridge has been balanced, any moment applied to the model unbalances the bridge and gives an output voltage directly proportional to the applied moment. When the moment is oscillatory, the resulting output signal is a modulated 3-kilocycle voltage whose modulation frequency is that of the applied moment or model oscillation frequency. The signal is then amplified by the linear amplifier and passed through a resolver which resolves the signal into two orthogonal components. (See ref. 8.) The reference component, or that part of the signal that is in phase with the resolver rotor, is called the real component. The quadrature component, or that part of the signal that is 90° out of phase with the resolver rotor, is called the imaginary component. The resolver is essentially a transformer having a single fixed primary winding and two secondary windings wound at right angles to each other on a rotor. The flux linkage of the rotor windings and, hence, the transformation ratio is proportional to the sine of the angle that the windings make with the flux produced by the primary winding current. Since the secondary windings are oriented 90° apart, the primary winding current when passed through the resolver is multiplied by $(\sin \omega_1 t)a$ in one secondary winding and by $(\cos \omega_1 t)a$ in the other secondary winding. The individual outputs are then demodulated to remove the 3-kilocycle carrier frequency from the signal. The resulting output currents are then read on direct-current microammeters of sufficient time constant to obtain the average value of each component.

The resolver, when rotated at the fundamental model frequency ω_1, plays an important part in the ability of the system to measure only the moment required to overcome the system damping even in the presence of random energy inputs such as those due to airstream turbulence and buffeting. The forcing function, or applied moment, under these conditions is nonsinusoidal and may be expressed by the Fourier series

$$M = M_o + \sum_{n=1}^{\infty} M_n \sin(n\omega_1 t + \lambda_n) \qquad (A4)$$

[redacted]

This forcing function occurs when there are an initial unbalance of the bridge M_o and harmonics due to the influence of stream turbulence or buffeting. The voltage applied to the resolver is then

$$e_M = BM \sin \omega_c t = BM_o \sin \omega_c t + B \sin \omega_c t \sum_{n=1}^{\infty} M_n \sin\left(n\omega_1 t + \lambda_n\right) \tag{A5}$$

Since the resolver is coupled to the model drive system and is driven at the fundamental frequency of the model, the demodulated output current for the real component is given by

$$i_{M_r} = A_{M_r} M_o \sin \omega_1 t + A_{M_r} \sin \omega_1 t \sum_{n=1}^{\infty} M_n \sin\left(n\omega_1 t + \lambda_n\right) \tag{A6}$$

The average value of the output current may be obtained by integrating equation (A6) over a long period of time, which is the process actually performed by the damped microammeters as shown in the following development.

The first term of equation (A6) can be produced by a static unbalance of the bridge and its average or integrated value is

$$\bar{i}_{M_r,o} = \lim_{\tau \to \infty} \frac{A_{M_r} M_o}{\tau} \left(1 - \cos \tau\right) = 0 \tag{A7}$$

Thus, any static unbalance of the bridge integrates to zero.

The average or integrated value of the second term of equation (A6), which includes the fundamental and all higher harmonics of the applied moment, is for $n = 1$

[redacted]

$$\bar{i}_{M_r,1} = \frac{A_{M_r} M_1}{2} \cos \lambda_1 \tag{A8}$$

and for $n \neq 1$

$$\bar{i}_{M_r,n} = \lim_{\tau \to \infty} \frac{A_{M_r} M_n}{2\tau} \left\{ \left[\frac{\sin(n-1)\tau}{n-1} - \frac{\sin(n+1)\tau}{n+1} \right] \cos \lambda_n + \left[\frac{\cos(n-1)\tau}{n-1} - \frac{\cos(n+1)\tau}{n+1} - \frac{2}{n^2-1} \right] \sin \lambda_n \right\} = 0 \tag{A9}$$

Thus, all random noise in the signal, at frequencies other than the fundamental, which may be produced by tunnel turbulence or buffeting, is integrated to zero (eq. (A9)). Equation (A8) includes only the average value of the real component of output current produced by the applied moment at the fundamental frequency of the resolvers ($n = 1$). The fundamental component of moment will contain a measure of any tunnel turbulence or buffeting energy which occurs at the frequency of oscillation ($n = 1$). But, since the input from turbulence and buffeting is random and the total energy involved is spread over a rather wide frequency spectrum, the energy remaining at the single discrete frequency of oscillation is infinitesimally small. Thus, the average or integrated value of moment current as measured still contains only the fundamental component of moment required to oscillate the model. The integration of the output currents is accomplished by applying the resolver output to a suitably damped microammeter. The fundamental component of moment is then indicated as a direct-current deflection of the meter needle and static unbalance of the bridge and any unwanted harmonics in the signal appear as damped fluctuations of the meter needle which may be visually averaged with time.

In a similar manner, the imaginary component of the moment current which is taken from the other terminals of the resolver, when integrated over time, gives

$$\bar{i}_{M_j,1} = \frac{A_{M_j} M_1}{2} \sin \lambda_1 \tag{A10}$$

[redacted]

When equation (A8) is multiplied by the calibration factor $\frac{2}{A_{M_r}}$, the real component of the applied moment (sketch 2) is given by

$$M_r = \frac{2\bar{i}_{M_r}}{A_{M_r}} = M_1 \cos \lambda_1 \tag{A11}$$

and, when equation (A10) is multiplied by $\frac{2}{A_{M_j}}$, the imaginary component is given by

$$M_j = \frac{2\bar{i}_{M_j}}{A_{M_j}} = M_1 \sin \lambda_1 \tag{A12}$$

The fundamental of the applied moment is then

$$M_1 = \sqrt{M_r^2 + M_j^2} \tag{A13}$$

and the phase angle that the fundamental component of the signal makes with the resolver rotor or reference axis (sketch 2) is given by

$$\lambda_1 = \tan^{-1} \frac{M_j}{M_r} \tag{A14}$$

[redacted]

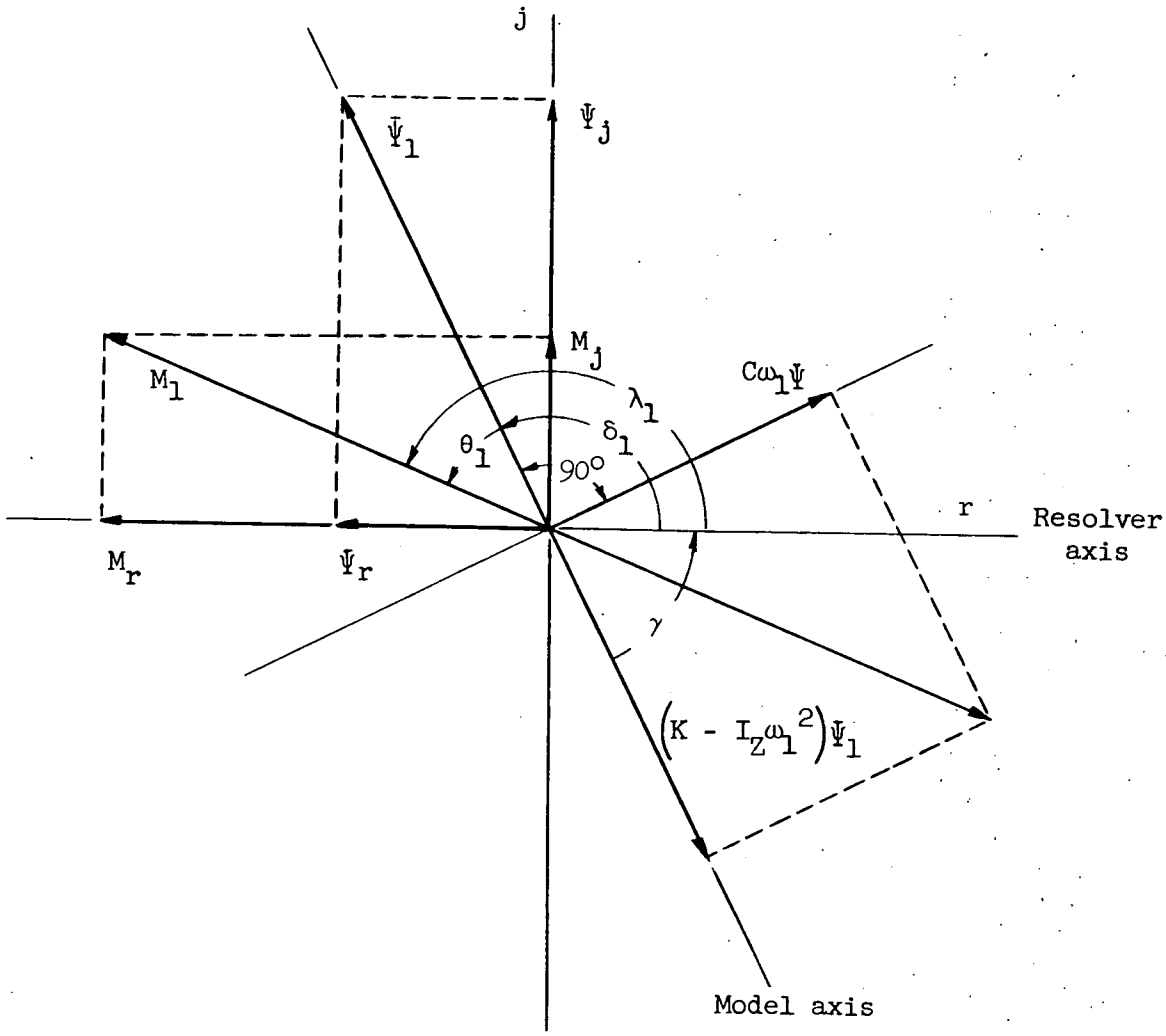

Sketch 2

A calibrated voltage proportional to the angular displacement of the model was supplied by a strain gage mounted on a flexible displacement beam which was connected between the oscillating model and the rigid support sting (figs. 1 and 2). The displacement output voltage was passed through a second resolver in a manner similar to that previously described for the moment signal. The angular displacement may therefore be determined as

$$\Psi_r = \frac{2\bar{i}_{\Psi_r}}{A_{\Psi_r}} = \Psi \cos \delta_1 \qquad \text{(A15)}$$

[redacted]

$$\Psi_j = \frac{2\bar{i}_{\psi_j}}{A_{\psi_j}} = \Psi \sin \delta_1 \tag{A16}$$

$$\Psi_1 = \sqrt{\Psi_r^2 + \Psi_j^2} \tag{A17}$$

$$\delta_1 = \tan^{-1}\left(\frac{\Psi_j}{\Psi_r}\right) \tag{A18}$$

The rotors of the moment and displacement resolvers are alined to be in phase but are set at an arbitrary angle γ with respect to the model axes (sketch 2). The angle γ includes any delay that may exist between the resolvers and the model.

From sketch 2, it is seen that the phase angle between the applied moment and angular displacement is given by

$$\theta_1 = \lambda_1 - \delta_1 = \tan^{-1}\left(\frac{M_j}{M_r}\right) - \tan^{-1}\left(\frac{\Psi_j}{\Psi_r}\right) \tag{A19}$$

and any time delay or phase angle γ between the drive motor and the model is subtracted out.

Oscillograph records were made of the angular frequency of the model during tests. These records were indexed by the operating circuit of the meter-recording cameras to insure that instantaneous values of oscillatory frequency f could be made simultaneously with the meter readings of moment and displacement. The angular velocity can then be determined as

$$\omega_1 = 2\pi f_1 \tag{A20}$$

Thus, with values of moment M_1, displacement Ψ_1, phase angle θ_1, and angular velocity ω_1, the system damping can be computed as

[redacted]

$$C_1 = \frac{M_1 \sin \theta_1}{\Psi_1 \omega_1}$$

and the system spring constant can be computed as

$$K_1 = \frac{M_1 \cos \theta_1}{\Psi_1} + I_Z \omega_1^2$$

Aerodynamic damping and aerodynamic spring constant or oscillatory directional stability were determined by subtracting the mechanical or tare characteristics of the system from the total system characteristics measured in the wind tunnel as follows:

$$C_{aero} = -\left[\left(\frac{M_1 \sin \theta_1}{\Psi_1 \omega_1}\right)_{\text{wind on}} - \left(\frac{M_1 \sin \theta_1}{\Psi_1 \omega_1}\right)_{\text{wind off}}\right] \tag{A21}$$

$$K_{aero} = -\left[\left(\frac{M_1 \cos \theta_1}{\Psi_1} + I_Z \omega_1^2\right)_{\text{wind on}} - \left(\frac{M_1 \cos \theta_1}{\Psi_1} + I_Z \omega_1^2\right)_{\text{wind off}}\right] \tag{A22}$$

These aerodynamic characteristics were reduced to coefficient form in the manner described in reference 2 so that the damping coefficient is

$$C_{n_r} - C_{n_{\dot{\beta}}} = \frac{C_{aero}(2V)}{qSb^2} \tag{A23}$$

and the oscillatory directional stability coefficient is

$$C_{n_\beta} + k^2 C_{n_{\dot{r}}} = \frac{K_{aero}}{qSb} \tag{A24}$$

[redacted]

It is pertinent to point out a factor which affects accuracy of measurement. As developed previously, system damping is expressed as

$$C = \frac{M_1 \sin \theta_1}{\Psi_1 \omega_1}$$

It is obvious in sketch 2 that, as the phase angle θ_1 between the moment vector M_1 and the displacement vector Ψ_1 approaches 90°, the variation of $\sin \theta_1$ with θ_1 is small, and high precision in the measurement of θ_1 is not required. Since a value of $\theta_1 = 90°$ corresponds to resonance (moment is in phase with velocity or 90° out of phase with displacement), for best accuracy measurements were made near the resonant condition.

[redacted]

APPENDIX B

DESCRIPTION OF MECHANICAL COMPONENTS OF MODEL AND DRIVE SYSTEM

The mechanism developed for these tests consisted of a sting-mounted model which was hydraulically forced to perform a single-degree-of-freedom angular oscillation about its vertical axis. A detailed description of the mechanism and of the pertinent factors involved in the design of its components is given in this appendix.

Motor Drive and Control

The hydraulic model oscillating system was driven by an externally mounted constant-speed, 1/2-horsepower, compound-wound, direct-current electric motor (figs. 2 and 4). Direct current was supplied to the motor by an alternating-current—direct-current motor generator set. Since accurate motor-speed control was mandatory for maximum data accuracy, motor speed was maintained constant by a self-compensating circuit which regulated generator output to the motor as a function of the pump drive-motor speed.

Hydraulic Drive Mechanism

Oscillating hydraulic pressure was supplied to the model drive piston by a hydraulic pump driven by the drive motor (figs. 2 and 4). The pump comprised a simple cam and piston and was connected to the model drive cylinder and piston by a single hydraulic line which passed through the model support sting (figs. 1 and 2). The hydraulic line was of thick-walled stainless-steel tubing. The tubing was of minimum practical length and inside diameter to minimize loss in fluid volume due to compression. (The tubing used for these tests had a 1/16-inch inside diameter and was 17 feet long.) Tubing having a smaller inside diameter caused unacceptable line losses due to viscous effects for these tests. All tubing joints and connections were smooth and fair to minimize fluid friction losses. The model drive piston was located in a cylinder in the support sting rearward of the model center of rotation and oscillated the model about the yaw pivot.

A coil spring was mounted opposite the drive piston between the model and the sting to return the model on the suction stroke of the hydraulic pump cycle. The mean value of internal hydraulic pressure was balanced by precompression of the coil spring and the model could be symmetrically centered about the sting center line by coil-spring tension adjustment (figs. 1 and 2).

[redacted]

A constant internal hydraulic pressure, independent of the oscillating pressure applied by the pump, was maintained on the hydraulic system by a pressure piston, lever arm, and differential weight (figs. 2 and 4). The constant-pressure system served to make up any hydraulic-fluid loss due to leakage past the "O" ring sealed pump, model drive, and constant-pressure pistons. The mass of the constant-pressure-system assembly was much greater than the mass of the model so that essentially only the model responded to oscillations of the hydraulic fluid.

Amplitude of the model oscillation was controlled by adjustment of the hydraulic-pump cam eccentric or stroke. Model oscillation amplitude was limited to a maximum of about $\pm 1^{\circ}$ by the available gap between the fuselage shell at the base and the support sting.

Frequency Springs

As mentioned previously, a coil spring was installed between the model and the sting to return the model on the suction stroke of the hydraulic pump cycle (figs. 1 to 3). The spring stiffness dictated the resonant frequency of the model. Maximum data accuracy resulted when the model was oscillated at its natural frequency (appendix A) and so springs of various stiffnesses were provided to permit a range of oscillation frequencies. Coil springs were used in this preliminary investigation because of the lack of available space in the model, even though the free ends of the coil springs contributed materially to the internal mechanical or tare damping. The amount of damping contributed by the free-end condition of the springs varied with the amount of precompression in the spring and thus considerable scatter occurred in the final data.

Flexure Pivot

Design of the model flexure pivot involved several important requirements. It was necessary that the pivot permit yawing motion and still withstand the normal force, chord force, side force, pitching moments, and rolling moments imposed at angles of attack up to $12\frac{1}{2}^{\circ}$ and dynamic pressures up to about 2,000 pounds per square foot. It was necessary that the pivot contribute minimum mechanical damping in order to reduce the wind-off or tare damping. The spring stiffness of the pivot had to be small so that the greater part of the total spring stiffness of the model would be contributed by the interchangeable frequency springs, and, thus, a greater range of frequency control would be afforded. In addition, the pivot was required to have a high resistance to fatigue failure. After considerable experimentation, a successful

flexure-pivot fabrication technique was evolved. The pivot comprised a cruciform arrangement of four 0.007-inch-thick flat beryllium-copper leaves installed radially in a hardened steel center post as shown in sketch 3.

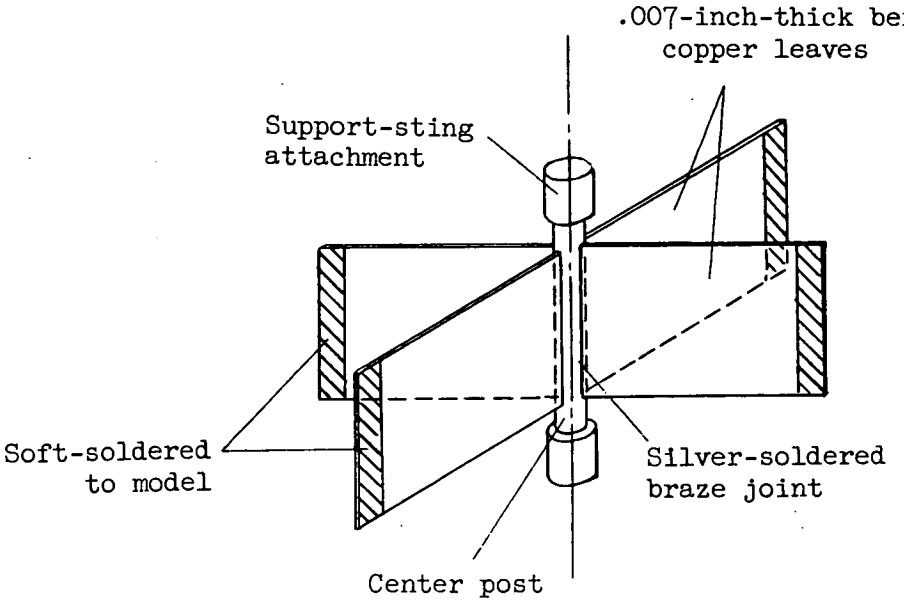

Sketch 3

The flexure pivot was assembled and the leaves brazed in the center post with powdered silver solder and cadmium. After the brazing operation, the beryllium-copper leaves were tempered to provide maximum strength and resistance to fatigue. The flexure-pivot assembly was then installed in the model with soft solder (figs. 1 to 3).

Model Force Beam

The model was forced to oscillate by the model piston which drove the model through a strain-gaged force beam (figs. 1 to 3). The force beam was made of aluminum and was designed to provide maximum strain or gage response for minimum total deflection. Thus, the rigid forcing requirement for this technique was met. (See appendix A.) The force beam was driven by the piston through a ball and socket joint so that strain applied to the gage beam was the result of a directly applied yawing moment only. The arrangement was of such a nature that the measured value of damping moment was independent of any normal-force, rolling-moment, or pitching-moment loads applied to the model. It is pertinent to point out that the force strain gage, when located at the model, is subjected only to those forces required to drive the model. Thus, the characteristics of the driving system do not affect the measured force.

[redacted]

Sting Support

The model sting was designed to have a high natural frequency so that the somewhat lower values of model oscillation frequency would not excite motion of the sting. In addition, all tests were made with the model center of gravity located on the model oscillation axis. The model and sting were, therefore, coupled only through the weak yaw flexure pivot and no appreciable sting motion resulted.

Amplifiers

Although any higher harmonics of the applied moment do not contribute to the direct-current moment output signals, as explained previously, the system amplifiers must pass these signals along with the fundamental component. The amplifiers must, therefore, have a large dynamic range.

REFERENCES

1. Fisher, Lewis R.: Experimental Determination of the Effects of Frequency and Amplitude on the Lateral Stability Derivatives for a Delta, a Swept, and an Unswept Wing Oscillating in Yaw. NACA RM L56A19, 1956.

2. Campbell, John P., Johnson, Joseph L., Jr., and Hewes, Donald E.: Low-Speed Study of the Effect of Frequency on the Stability Derivatives of Wings Oscillating in Yaw With Particular Reference to High Angle-of-Attack Conditions. NACA RM L55H05, 1955.

3. Cahill, Jones F., and Bird, John D.: Low-Speed Tests of a Free-To-Yaw Model in Two Wind Tunnels of Different Turbulence. NACA RM L51L14, 1952.

4. Palmer, William E.: A Wind-Tunnel Investigation of the Low-Amplitude Damping in Yaw and Directional Stability of a Fuselage-Tail Configuration at Mach Numbers Up to 1.10. NACA RM L57C15, 1957.

5. Beam, Benjamin H.: A Wind-Tunnel Test Technique for Measuring the Dynamic Rotary Stability Derivatives at Subsonic and Supersonic Speeds. NACA Rep. 1258, 1956. (Supersedes NACA TN 3347.)

6. Queijo, M. J., Fletcher, Herman S., Marple, C. G., and Hughes, F. M.: Preliminary Measurements of the Aerodynamic Yawing Derivatives of a Triangular, a Swept, and an Unswept Wing Performing Pure Yawing Oscillations, With a Description of the Instrumentation Employed. NACA RM L55L14, 1956.

7. Von Doenhoff, Albert E., and Horton, Elmer A.: A Low-Speed Experimental Investigation of the Effect of a Sandpaper Type of Roughness on Boundary-Layer Transition. NACA TN 3858 (Corrected copy), 1956.

8. Lessing, Henry C., Fryer, Thomas B., and Mead, Merrill H.: A System for Measuring the Dynamic Lateral Stability Derivatives in High-Speed Wind Tunnels. NACA TN 3348, 1954.

[redacted]

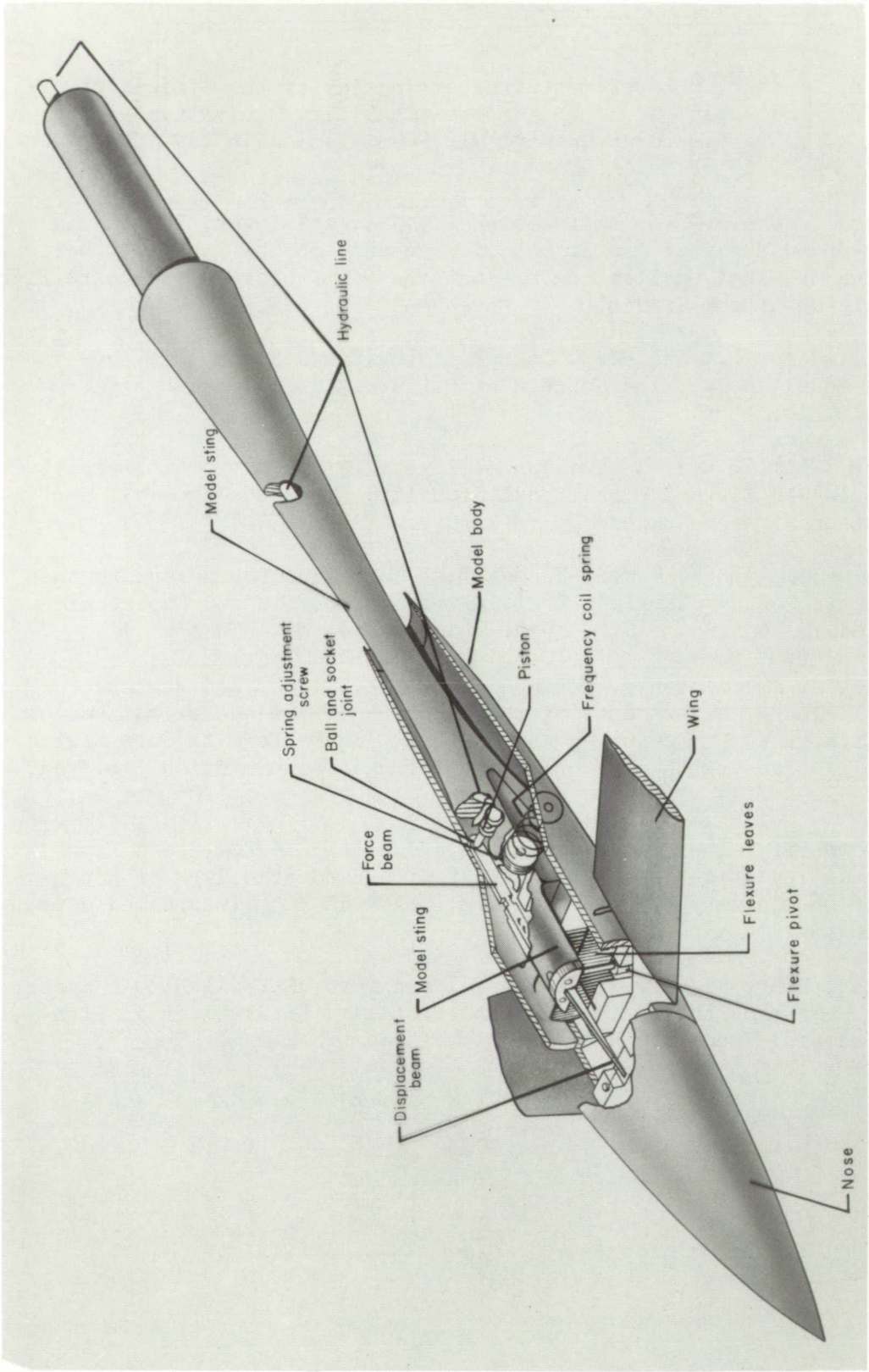

Figure 1.- Isometric sketch of model, internal mechanism, and sting support. L-57-167

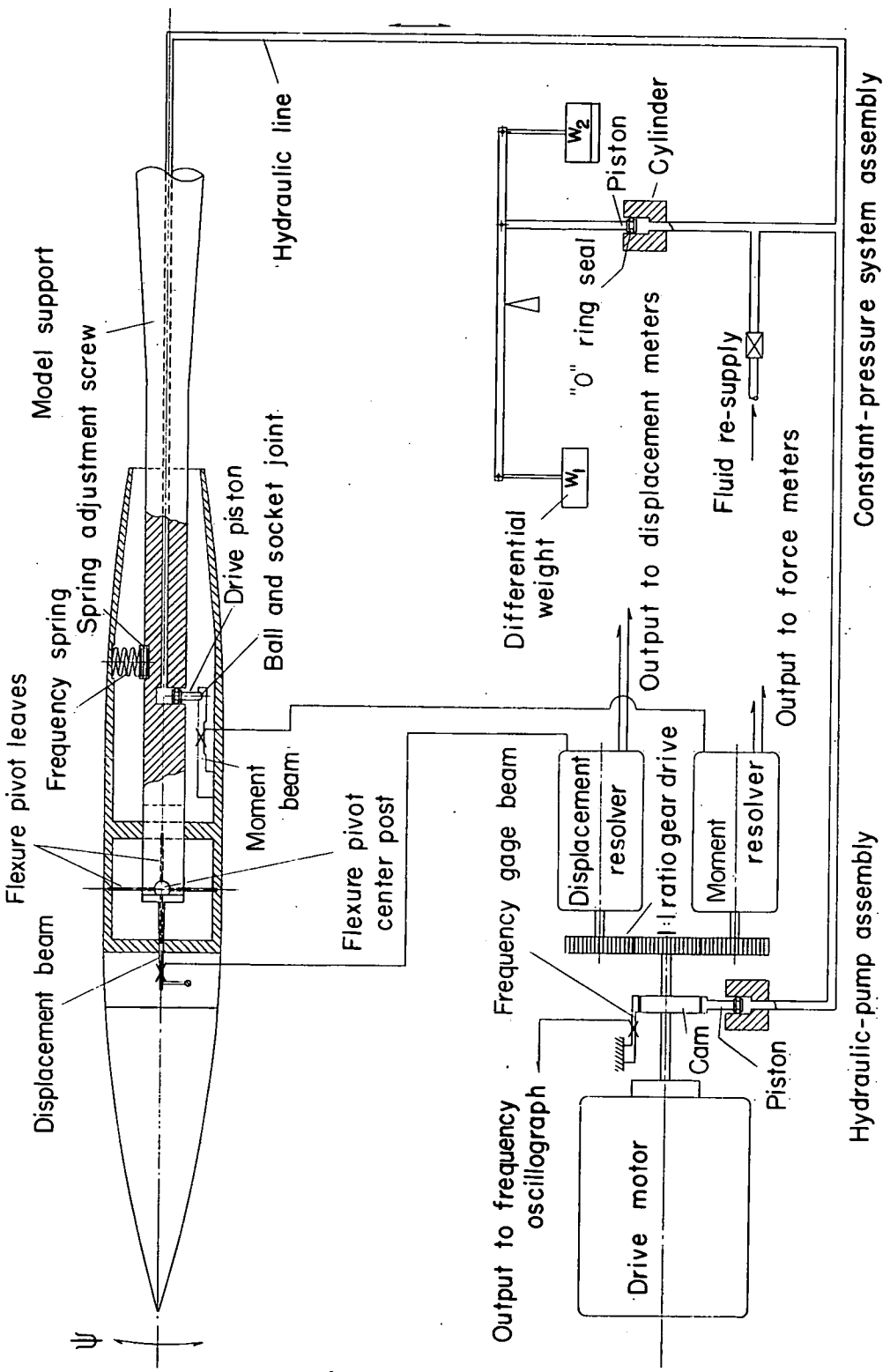

Figure 2.- Sketch of model and driving system components.

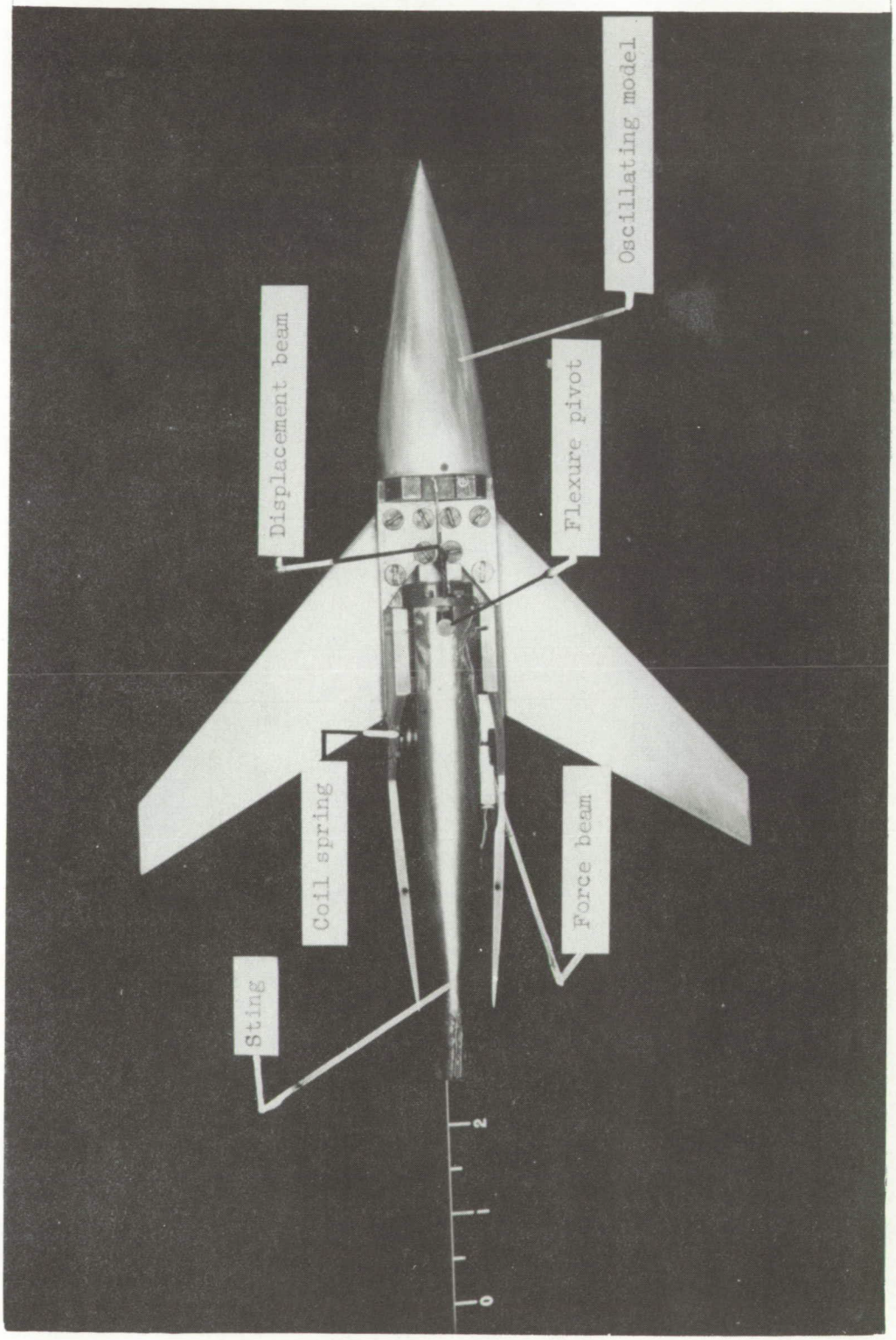

Figure 3.- Model and internal mechanism. L-96055.1

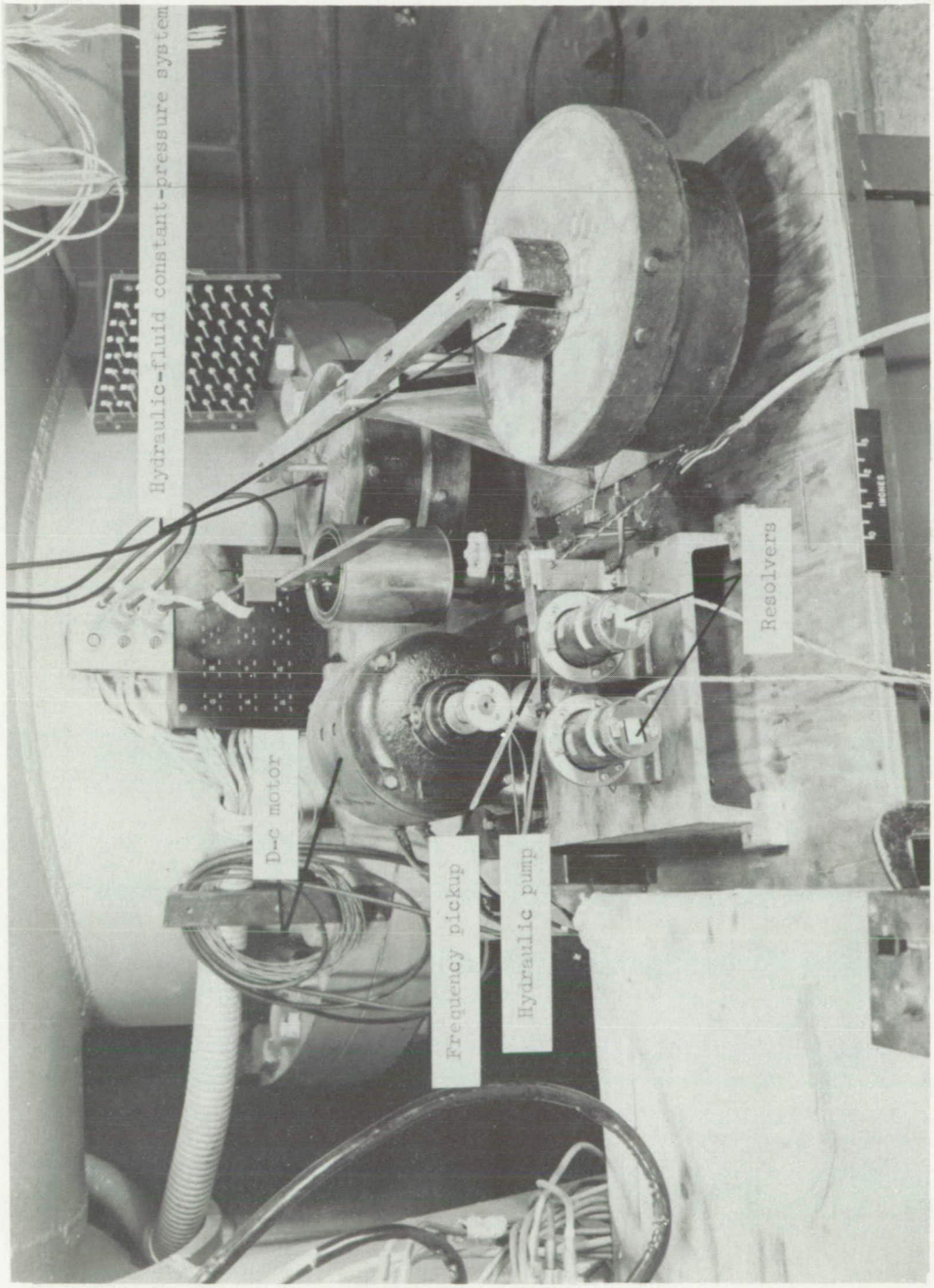

L-96053.1

Figure 4.- Externally mounted motor drive, hydraulic pump and components, and resolvers.

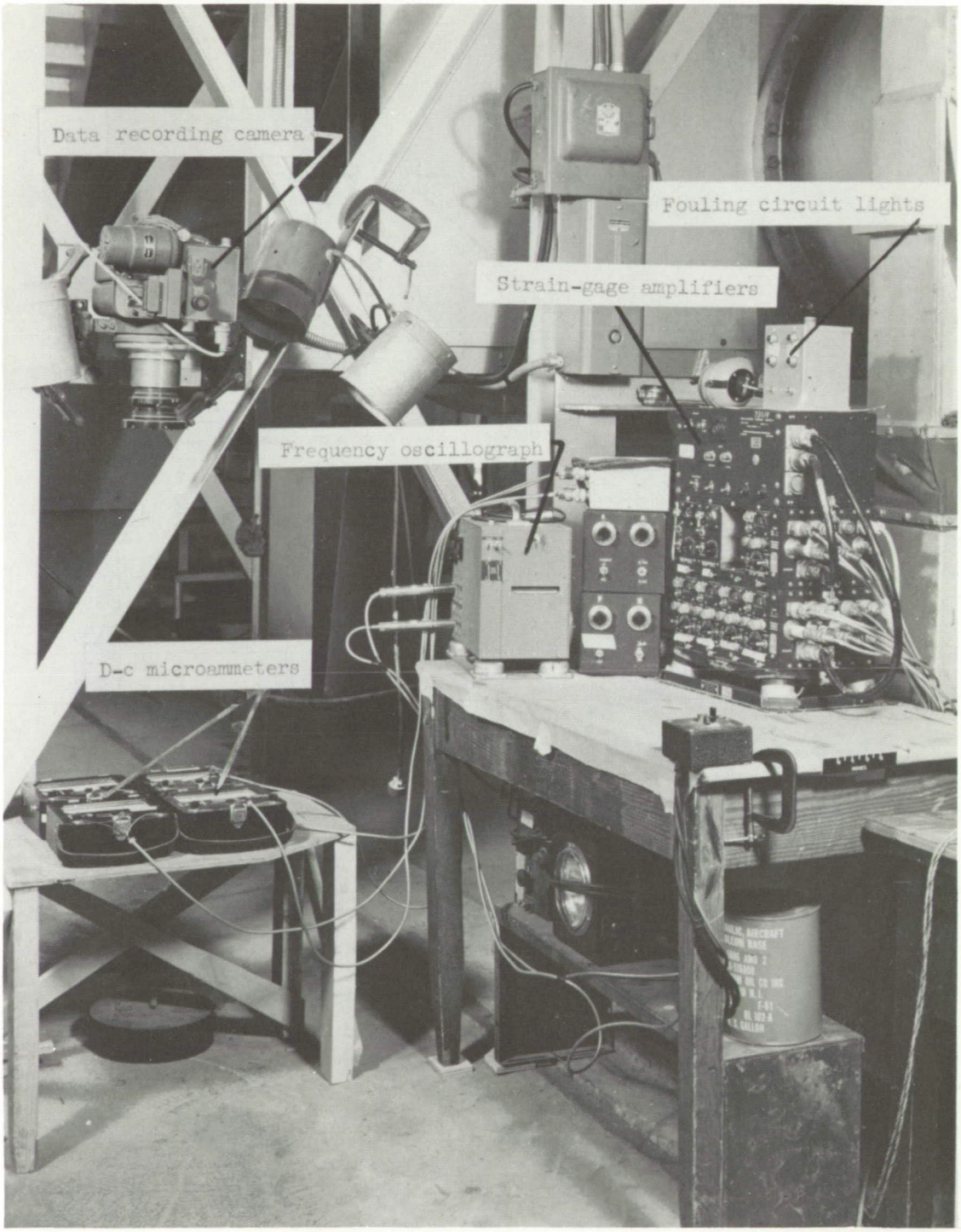

Figure 5.- Electrical instrumentation. L-96052.1

[redacted]

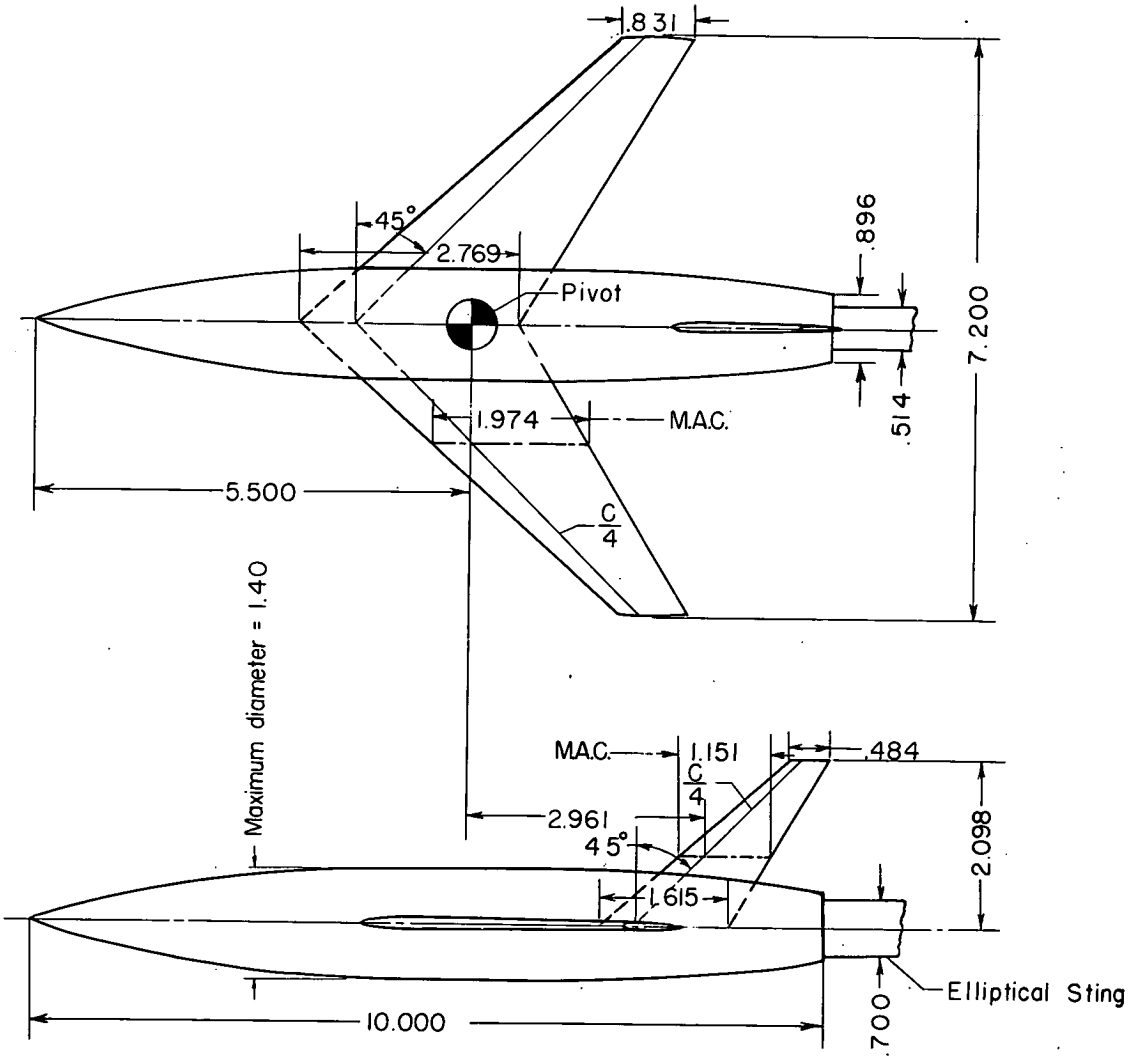

Figure 6.- Sketch of model. (All dimensions in inches.)

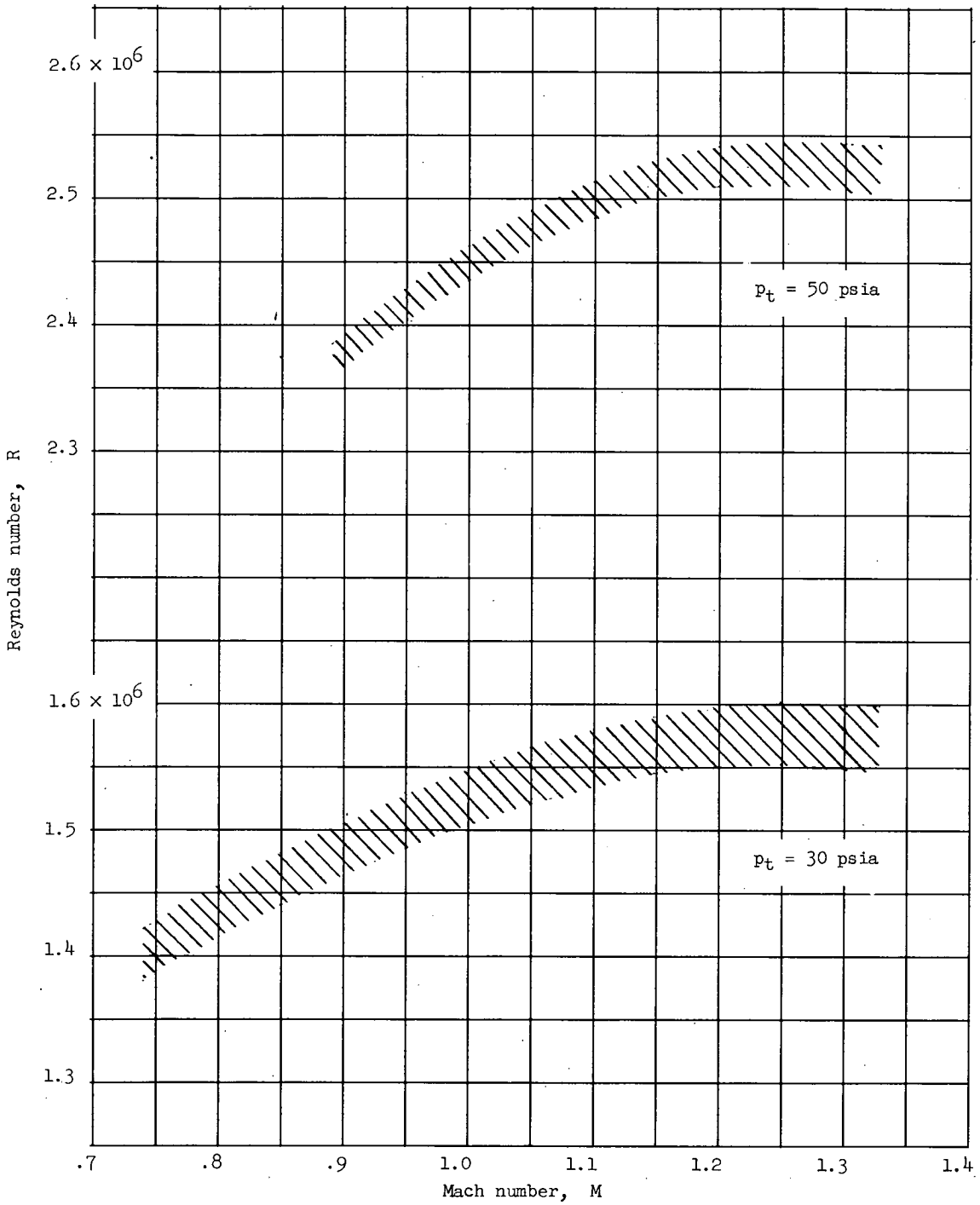

Figure 7.- Variations of Reynolds number with Mach number at constant wind-tunnel stagnation pressures.

[redacted]

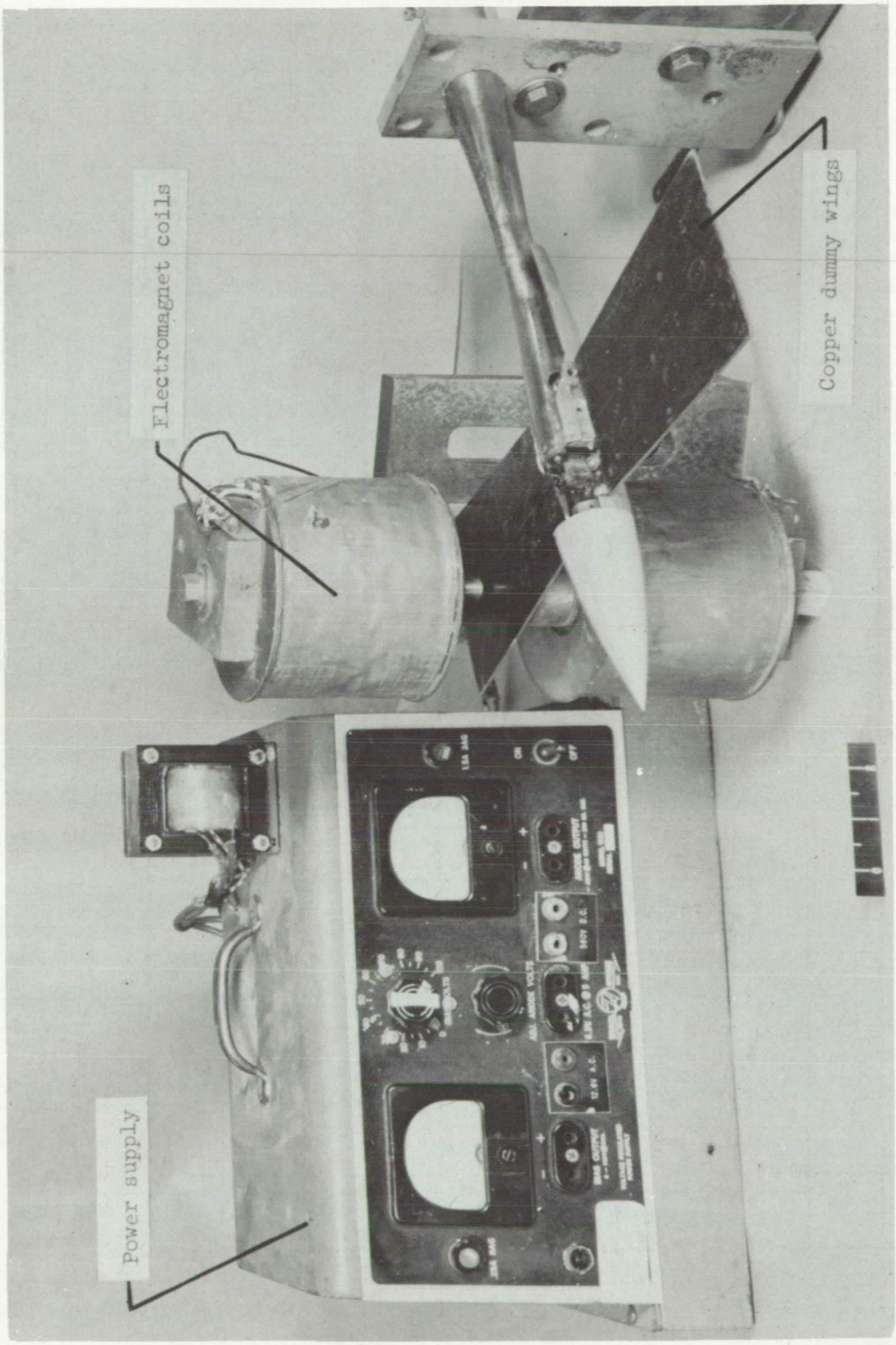

Figure 8.- Model with electromagnetic eddy-current damper installed. L-96638.1

[redacted]

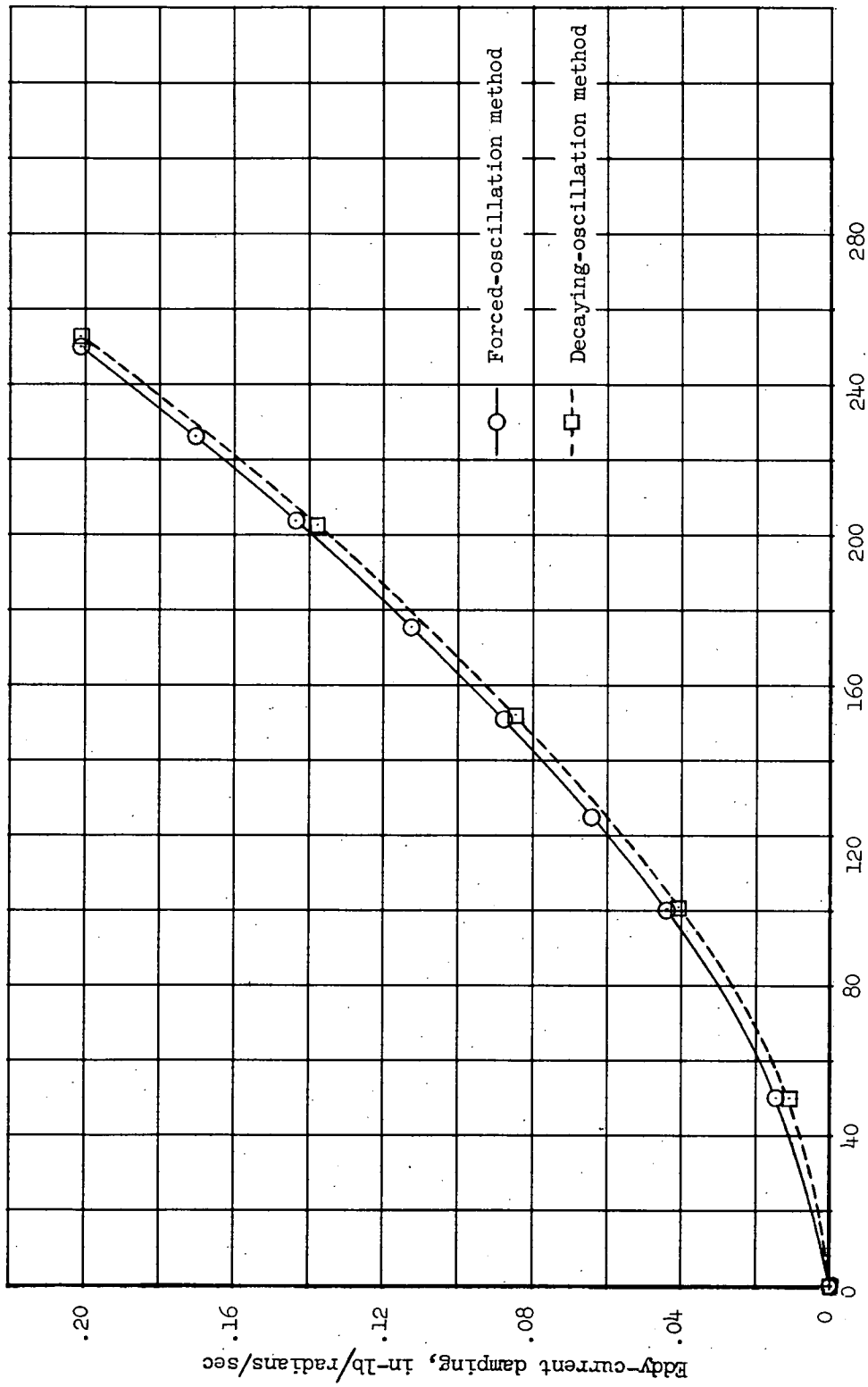

Figure 9.- Variation of measured eddy-current damping moment with damper coil current as determined by the free-decay and force-driven techniques.

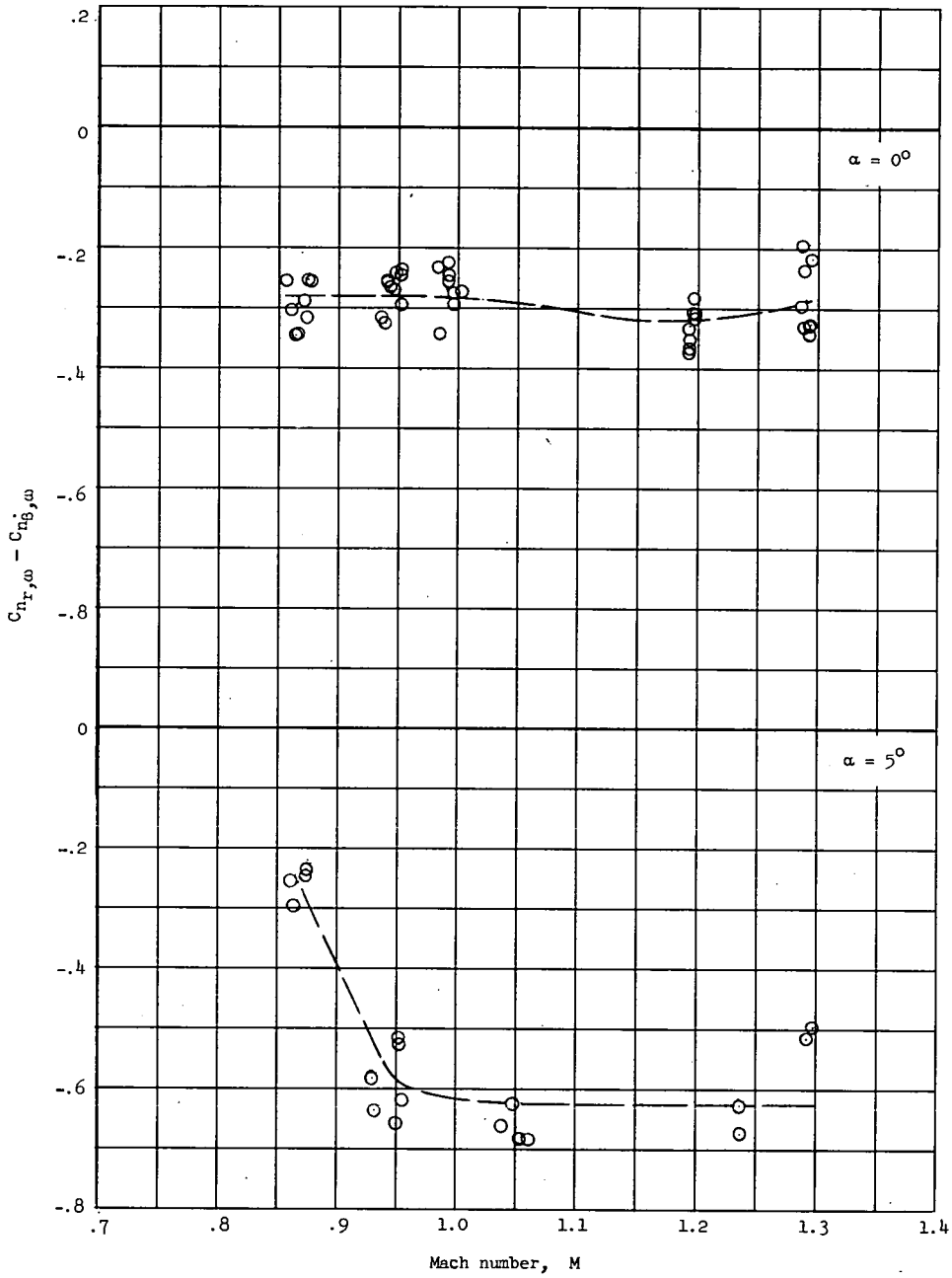

(a) Frequency spring 1; p_t = 30 psia; $\frac{\omega b}{2V}$ = 0.038 to 0.057.

Figure 10.- The variation of the damping-in-yaw derivative $C_{n_{r,\omega}} - C_{n_{\dot{\beta},\omega}}$ with Mach number.

[redacted]

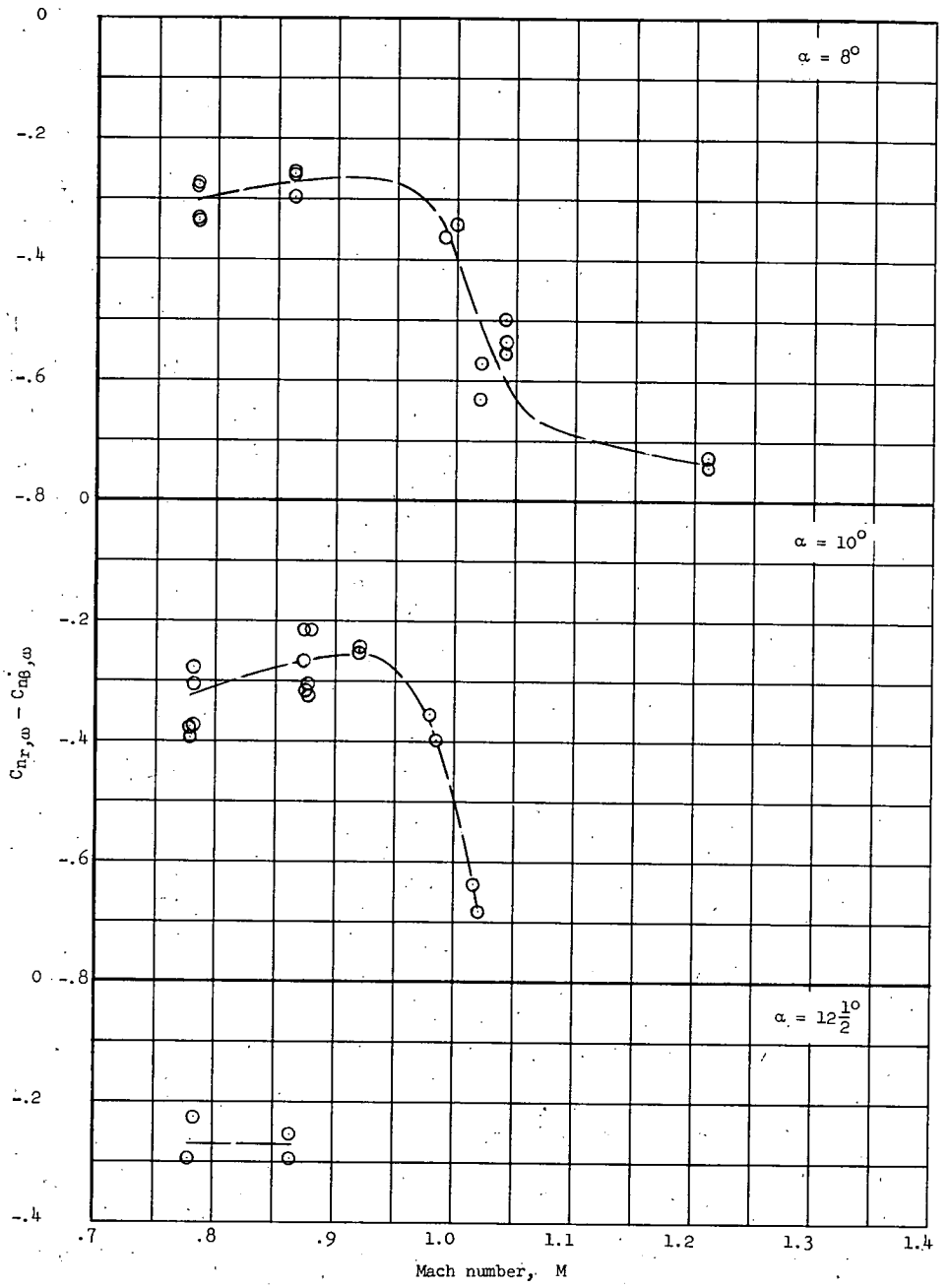

(a) Concluded.

Figure 10.- Continued.

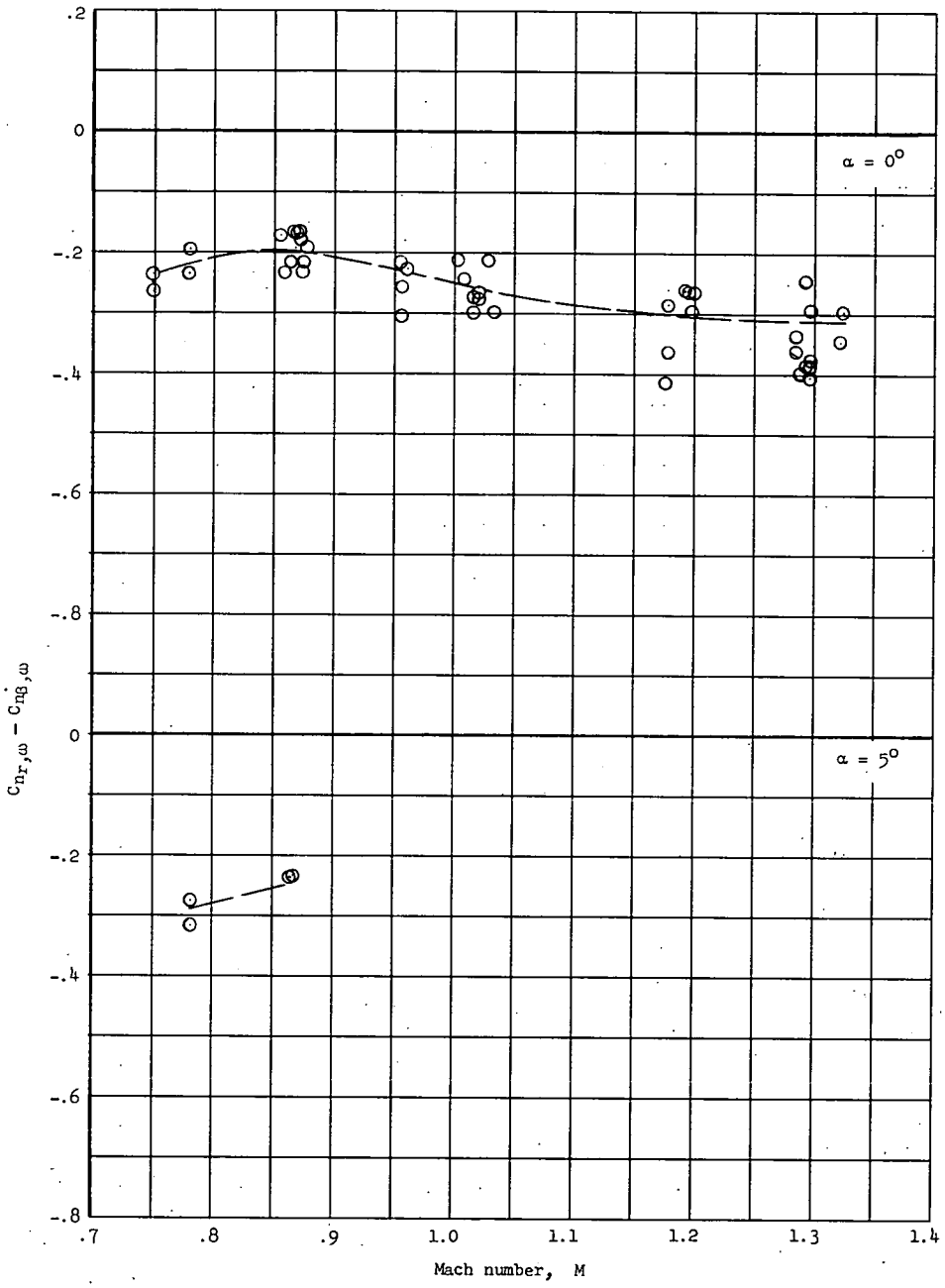

(b) Frequency spring 2; p_t = 30 psia; $\frac{\omega b}{2V}$ = 0.034 to 0.049.

Figure 10.- Continued.

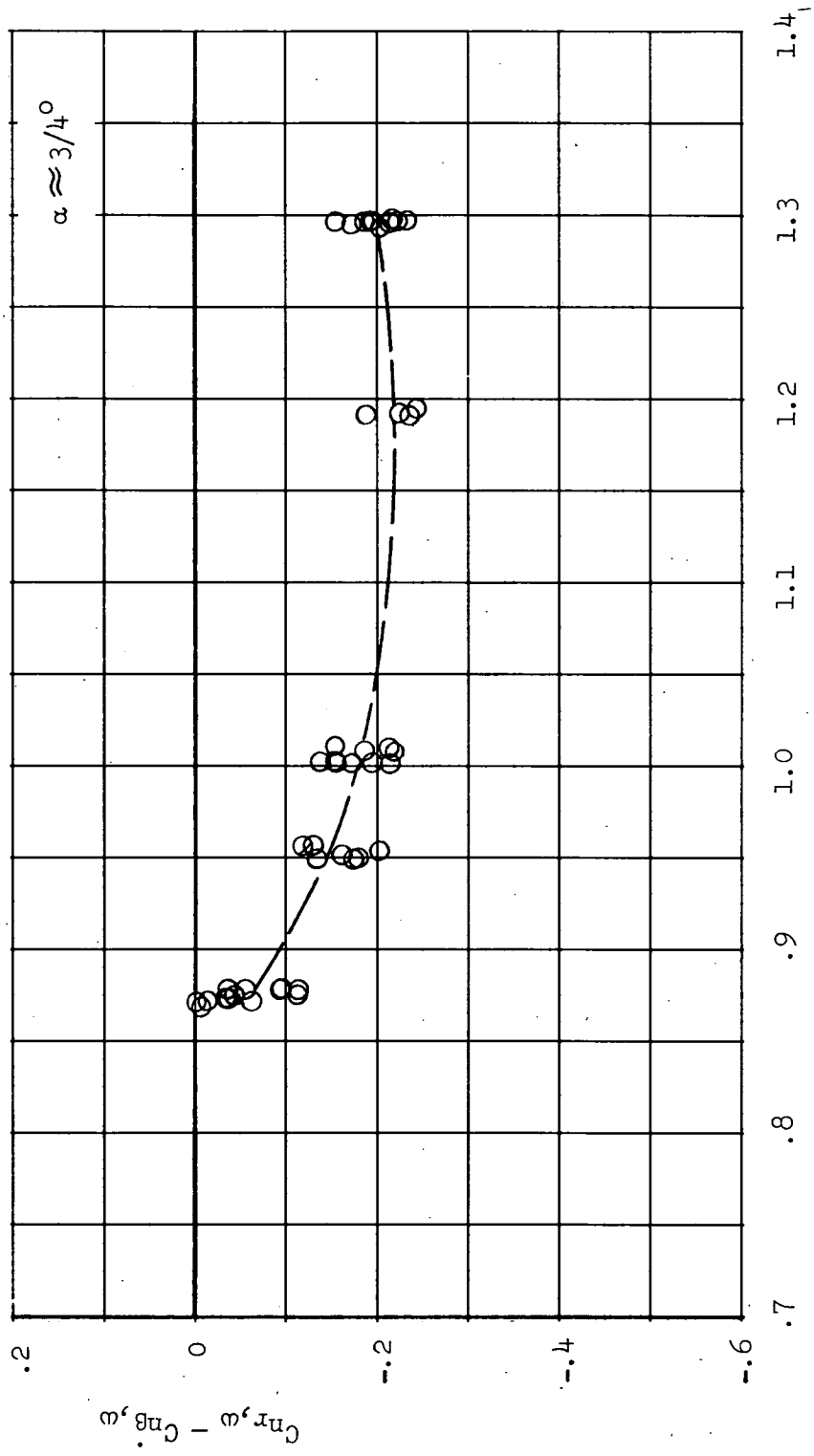

(c) Frequency spring 3; p_t = 30 psia; $\frac{\omega b}{2V}$ = 0.030 to 0.039.

Figure 10.- Continued.

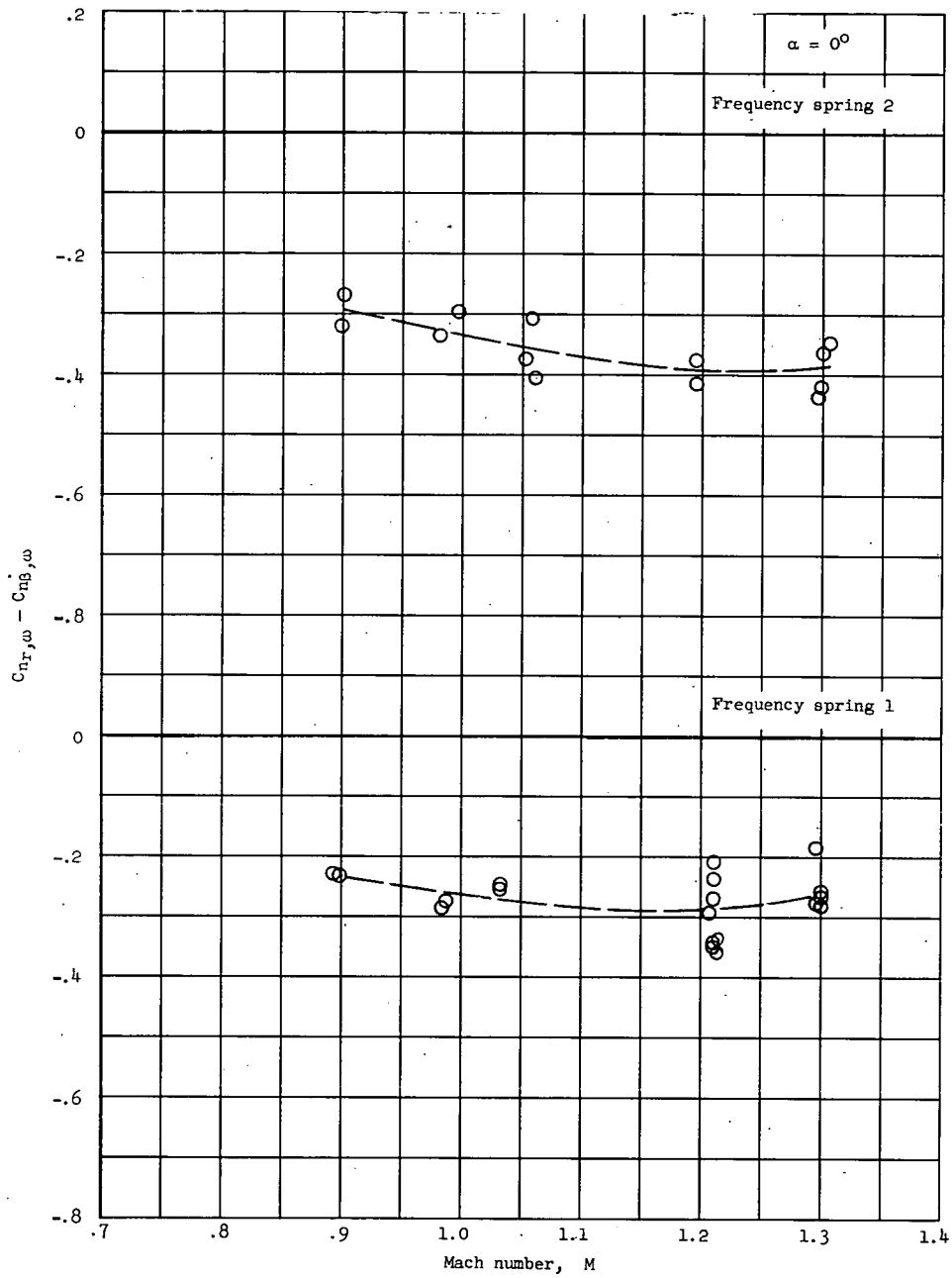

(d) Frequency springs 1 and 2; p_t = 50 psia; $\frac{\omega b}{2V}$ = 0.037 to 0.051.

Figure 10.- Concluded.

[redacted]

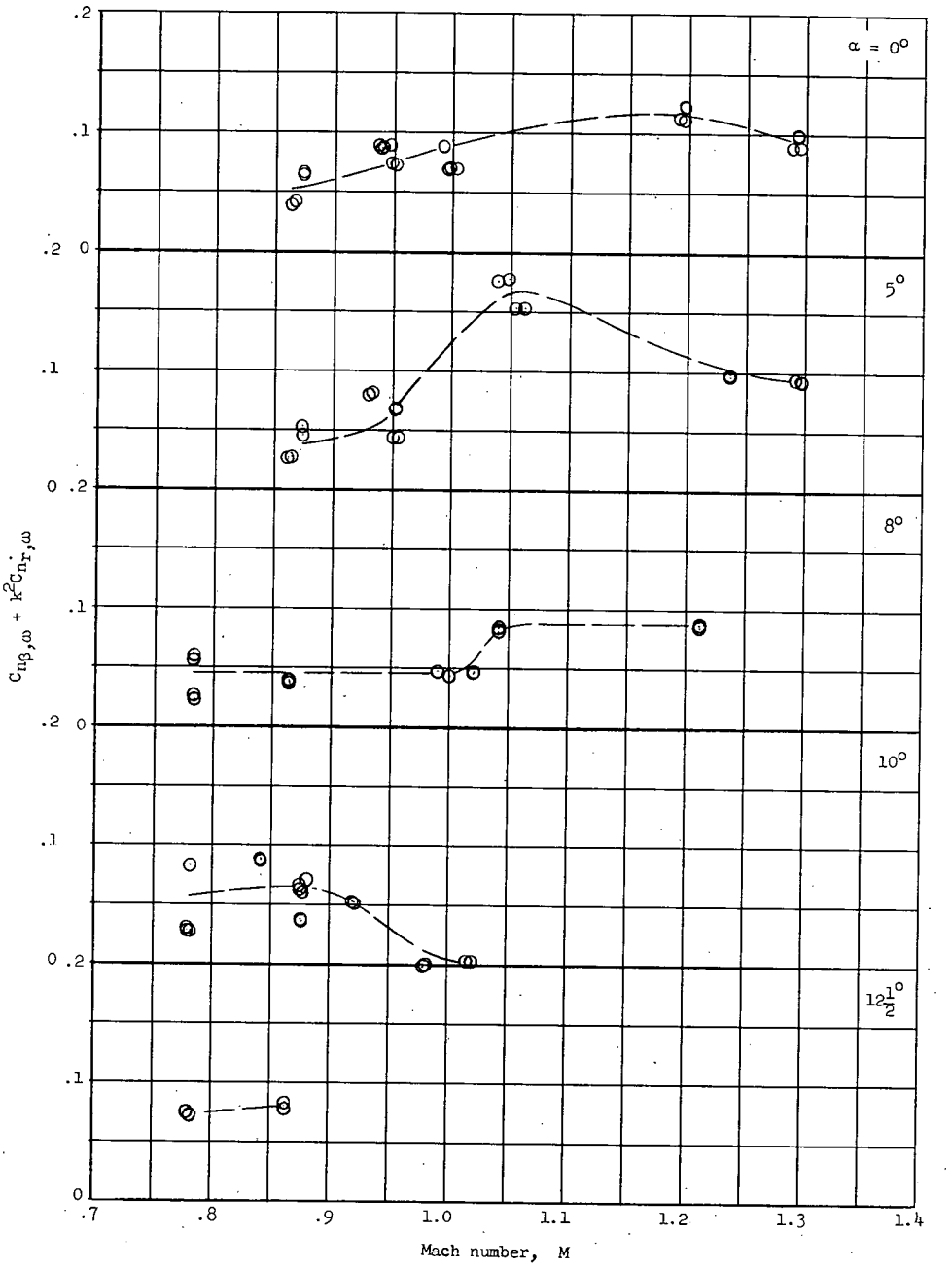

(a) Frequency spring 1; p_t = 30 psia; $\frac{\omega b}{2V}$ = 0.038 to 0.057.

Figure 11.- The variation of oscillatory directional stability derivative $C_{n_{\beta,\omega}} + k^2 C_{n_{\dot{r},\omega}}$ with Mach number.

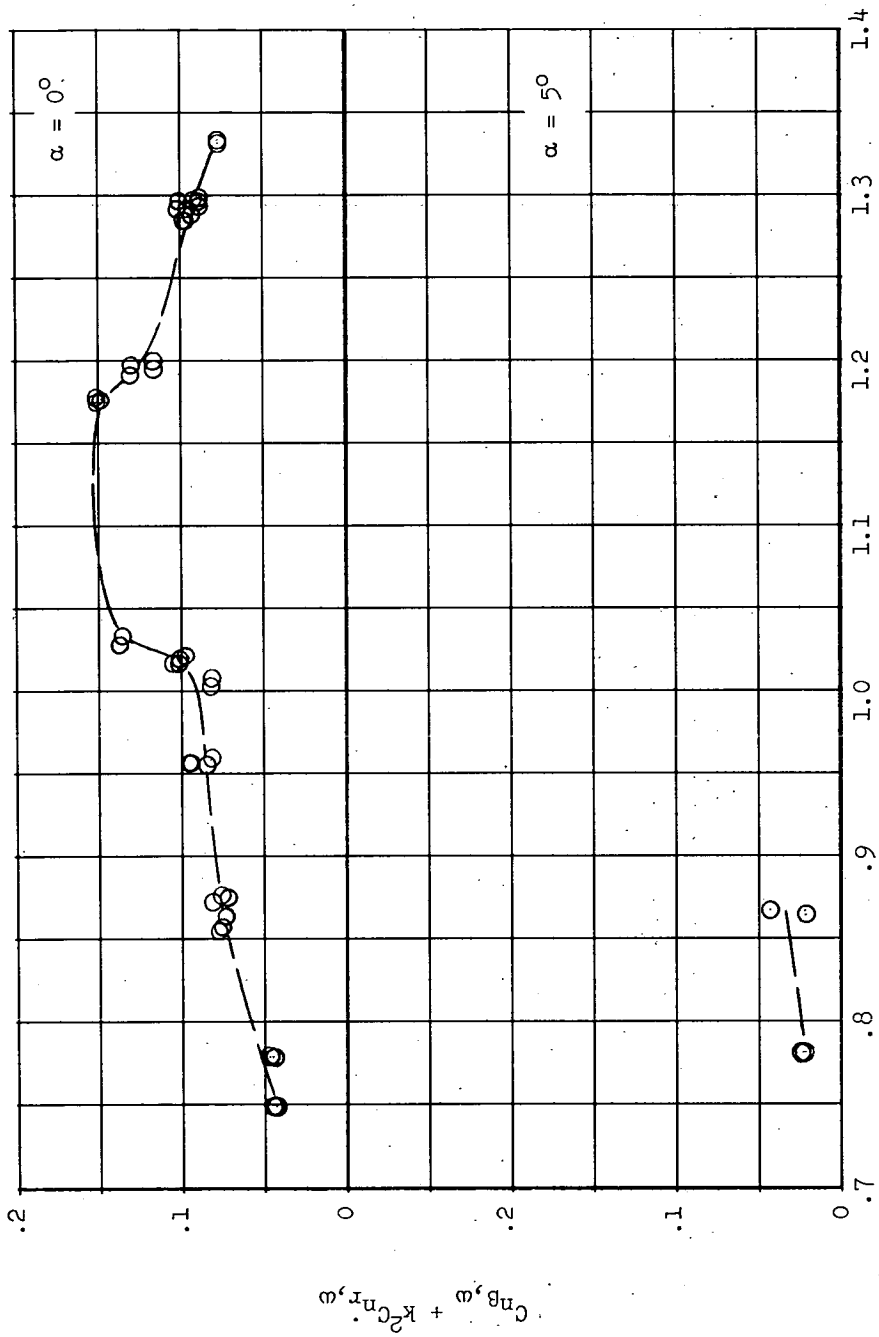

(b) Frequency spring 2; p_t = 30 psia; $\frac{\omega b}{2V}$ = 0.034 to 0.049.

Figure 11.- Continued.

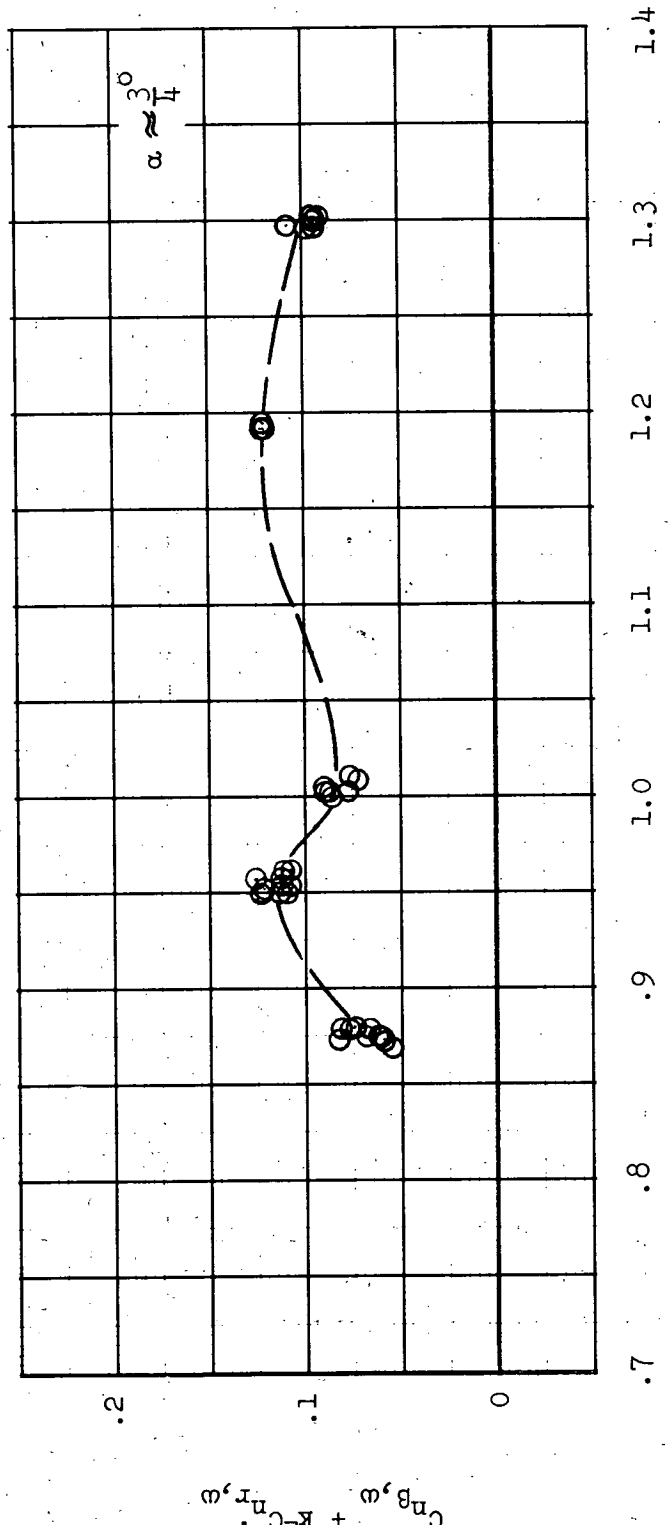

(c) Frequency spring 3; p_t = 30 psia; $\frac{\omega b}{2V}$ = 0.030 to 0.039.

Figure 11.- Continued.

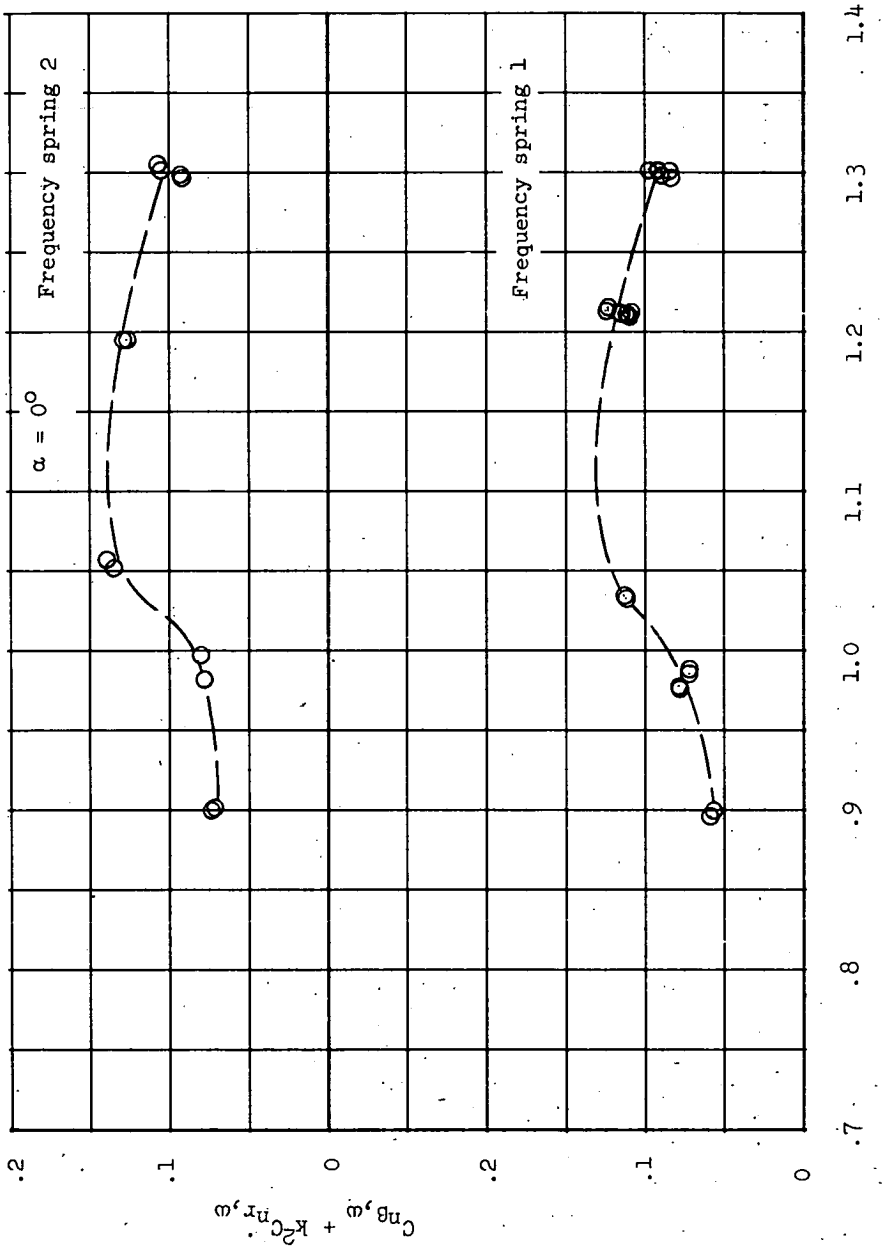

(d) Frequency springs 1 and 2; p_t = 50 psia; $\frac{\omega b}{2V}$ = 0.037 to 0.051.

Figure 11.- Concluded.

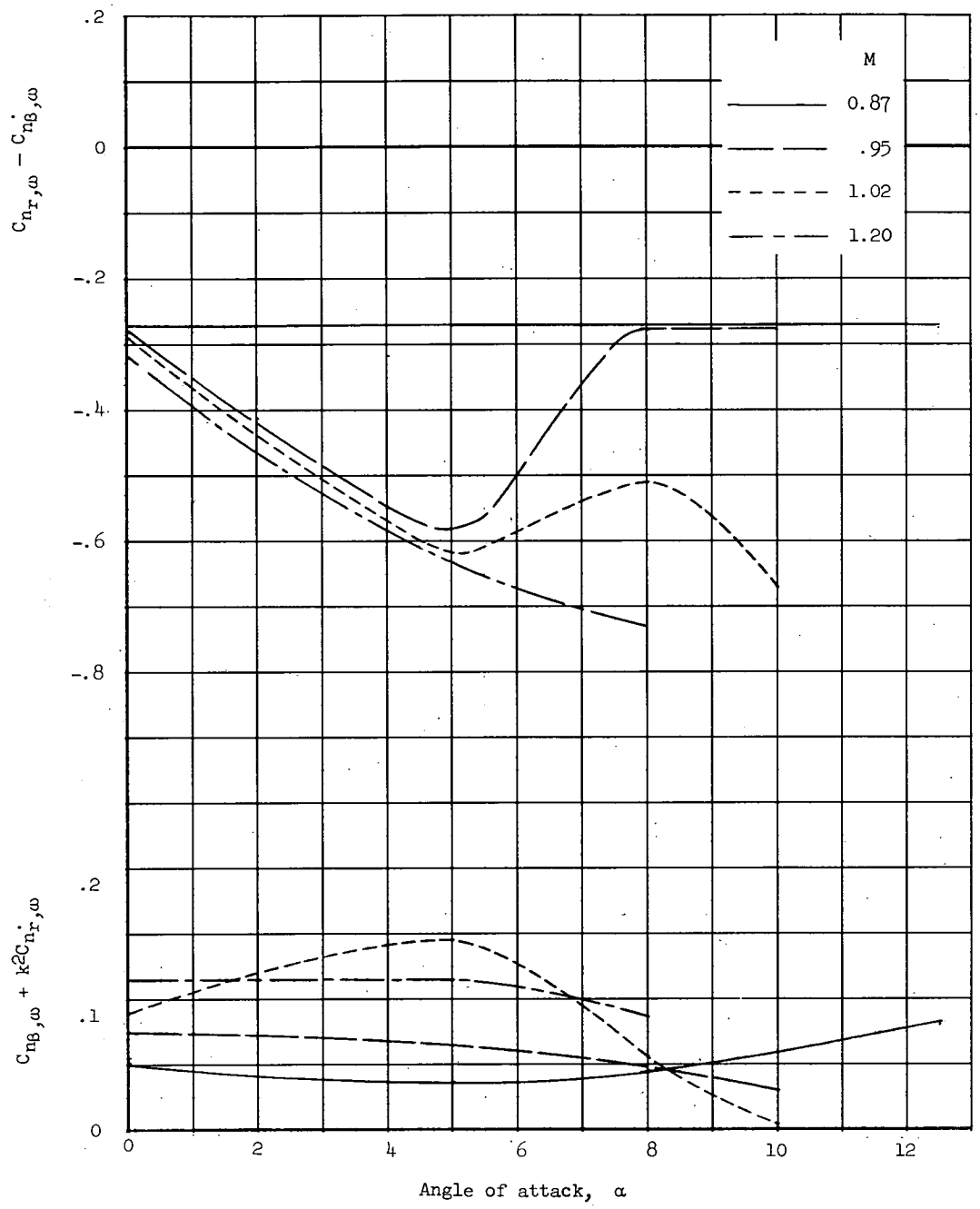

Figure 12.- The variations of $C_{n_{r,\omega}} - C_{n_{\dot{\beta},\omega}}$ and $C_{n_{\beta,\omega}} + k^2 C_{n_{\dot{r},\omega}}$ with angle of attack for various Mach numbers. Frequency spring 1; p_t = 30 psia; $\frac{\omega b}{2V}$ = 0.042 to 0.052.

[redacted]

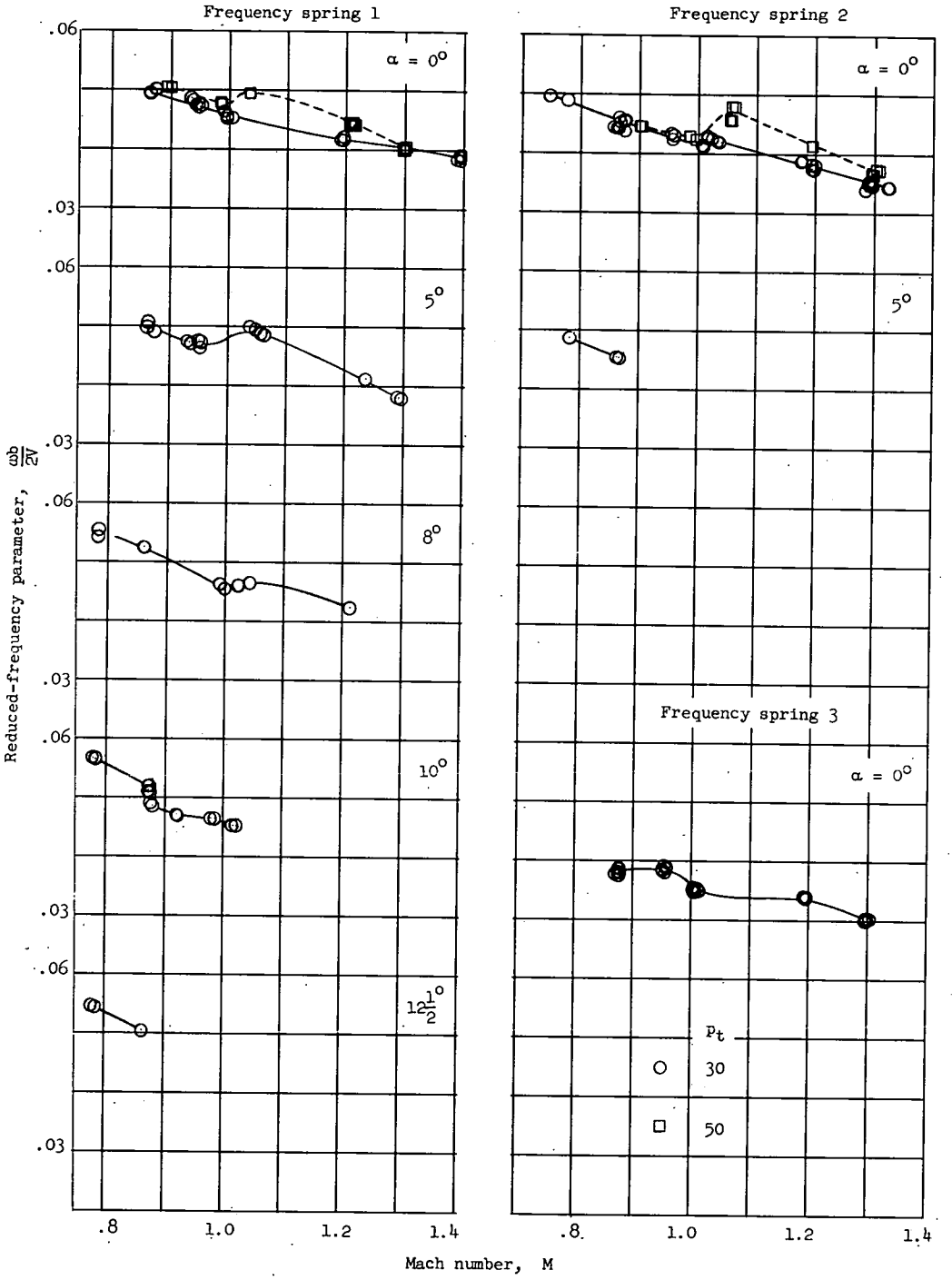

Figure 13.- The variation of reduced-frequency parameter $\frac{\omega b}{2V}$ with Mach number for various test conditions.

[redacted]

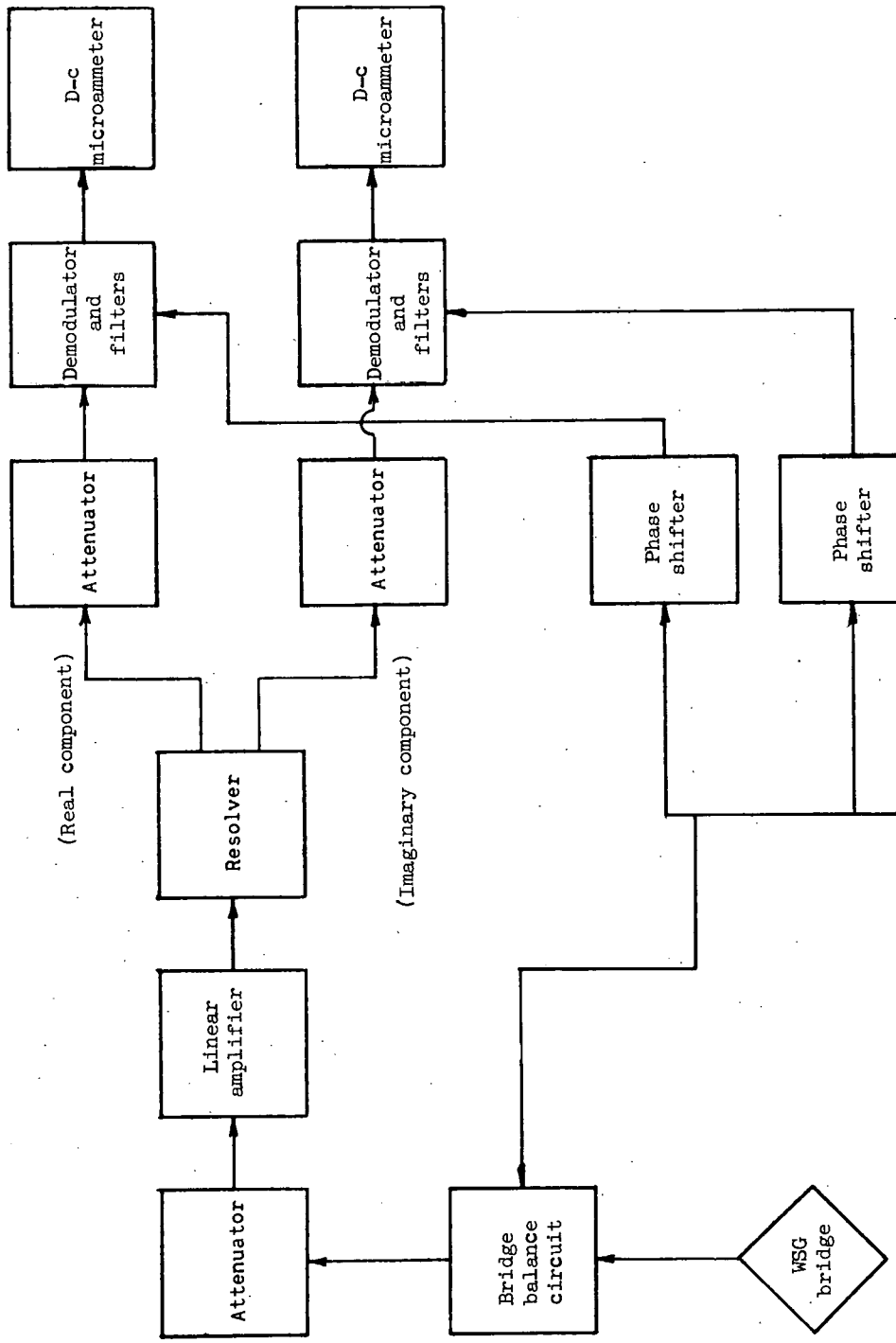

Figure 14.- Block diagram of electronic circuits used to measure model displacement and applied moment.